Assessment of Photovoltaic Integration on Metro Wagon Surfaces in Amsterdam

Tristan ten Napel

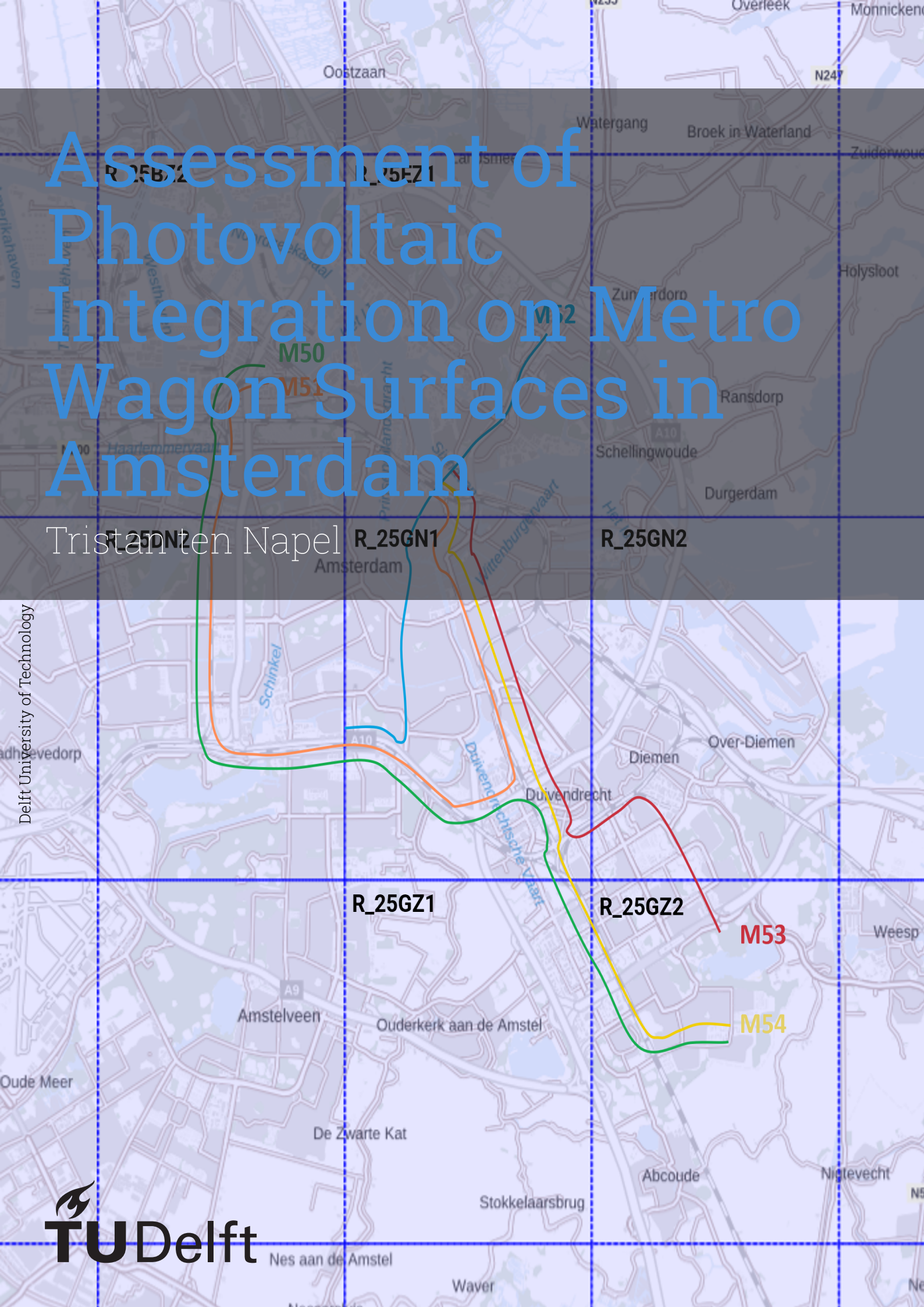

Delft University of Technology

TU Delft

Assessment of Photovoltaic Integration on Metro Wagon Surfaces in Amsterdam

by

Tristan ten Napel

to obtain the degree of Master of Science
at the Delft University of Technology,
to be defended publicly on Friday May 2nd, 2025 at 13:00 PM.

Student number:	4593219	
Project duration:	November, 2023 – May, 2025	
Thesis committee:	Dr. ir. H. Ziar,	TU Delft, supervisor
	Prof. dr. ir. A. H. M. Smets,	TU Delft
	Dr. M. Cvetkovic,	TU Delft

An electronic version of this thesis is available at http://repository.tudelft.nl/.

TU Delft

Preface

Dear reader!

Thank you for taking the time to read this report on my master's thesis. What you have before you is the result of many months of very hard work. It took a little bit longer than originally intended, *maar*, *wat is*, *dat is*! Besides working on the thesis 4 days a week, the other weekday and many evenings were reserved for my two side-jobs. Being an active member in two committees at my association as well, meant that I unfortunately burnt out a couple of times. The prouder I am today for actually finishing the thesis!

Although at times everything seemed bleak, I never intended to give up. And that would not have been possible without the help and continuous support of my friends, family and others. I would like to thank two people in particular. First, my supervisor, Hesan Ziar. Thank you for all the fruitful, lengthy and *gezellige* discussions on my research and, most important, non-research, whether that be physics or our personal lives. Thank you for all the times you helped me out when I was stuck with the project and when you supported me and helped me regain my motivation. I always left your office a more confident man than when I entered. The same goes for the meetings with my student counselor, Paula Leenders-Bresser. Whether we met in EWI, 2WI, or during certain years even via Zoom, I am forever grateful for all the times you helped me. Time and time again when I had lost trust in my self, you reminded and convinced me of my skills.

To think that I would be able to produce a ginormous computer model (let alone in MATLAB!), would have been unthinkable not too long ago. My friends from my bachelor of Applied Physics probably still cannot fathom this. To them specifically: did you know that nowadays I can operate the TU Delft printers too?

I am incredibly proud with the result you have in front of you. It would not have been possible without all of my friends and family. So once again, I want to thank each and everyone of you. Happy reading!

Wel gelachen,
Tristan ten Napel
Delft, 24 April 2025

Abstract

The Dutch national sustainability goals are too ambitious for current government plans. Reaching these goals can become even harder than it already is, as the Dutch government faces two challenges that are especially present in the Netherlands. These problems are increasing grid congestion and NIMBY's contesting the use of land for renewable energy production. Novel, decentralized integrated photovoltaic technologies (PV) can potentially tackle both problems at once. Building-integrated PV (BIPV) and vehicle-integrated PV (VIPV) are examples of this. This research focuses on VIPV. VIPV poses some unique challenges compared to stationary PV systems. Being a dynamic system, shading and module orientation change rapidly over time, whereas for a stationary system these are both optimized for the highest yield results.

This research investigates the **feasibility of photovoltaic integration on metro wagon surfaces in the Amsterdam metro network**. To this end, an extensive MATLAB model was made. The model uses inputs from sources such as from GVB[1], KNMI[2] and PDOK[3]. The model is designed to output the potential yield for metro trains running on the five different metro lines consisting of GVB's metro network.

The model uses five submodels: a skyline, a metro position, a weather, a temperature and a yield model. The skyline model produced a library of 456 skyline profiles along the aboveground sections of the metro net. The metro position model estimates the positions of the metro trains by using timetables directly from the GVB website. The weather model parses KNMI data and determines the module irradiance using both a BRL and Perez model. The temperature model uses a fluid-dynamic model to model the module temperature and distinguishing between the contributions of the different heat fluxes. The yield model calculates the variable efficiency of the modules and consequently their yield.

The output data is stored in cell arrays. For each of the five metro lines, for each of their two directions, trains were subdivided into three segments and the roof of each segment was subdivided into three sections. Each of these cells contain matrices of 365x5000, the rows representing the days of the year and the columns the amount of timestamps. The three rooftop sections represent the slanted sections on both the port and starboard side of the vehicle (w.r.t. the outbound driving direction) and the flat section in the middle.

Probability distributions of the yield, timestamps and Sky View Factor (SVF) were produced. Besides providing insight in the behavior of the PV system, these also show the amount of instances where the yield and the SVF are 0, representing the amount of minutes where the modules are fully covered by tunnels, viaducts or train station roofs.

The total yield for each of the metro lines varies greatly: 301 MWh for Line 50, 173 MWh for Line 51, 79.8 MWh for Line 52, 91.8 MWh for Line 53 and 108 MWh for Line 54. The differences are explained by the aboveground percentages and the train frequencies on each line. The specific yields range from $\sim$590kWh/kWp for the flat roof section on Line 50 and between $\sim$66 and 82 kWh/kWp for the slanted roof section on the starboard section on Line 52. A heatmap was produced showing the annual yield in kWh/m^2 as a function of location for each of the lines, distinguishing between roof sections. The specific yields show that integration is most feasible for Line 50, followed by 51, 54, 53 and 52 respectively. For economic viability, lower specific yields mainly mean a longer payback period, so the choice is up to the GVB if they deem the costs worth the benefits. In conclusion, this model shows promising results for the feasibility of integrating PV modules on the Amsterdam metro network

[1]The GVB is the operator of the Amsterdam metro network. GVB used to be short for Gemeentevervoerbedrijf, but after it stopped being an official "gemeentebedrijf", it kept the name GVB without being an official abbreviation anymore.

[2]Koninklijke Nederlands Meteorologisch Instituut, or Royal Netherlands Meteorological Institute

[3]Publieke Dienstverlening Op de Kaart is a government service that provides free access to geobasis registrations and other geodatasets.

Contents

List of Figures

List of Tables

1

Introduction

1.1. Motivation

In both the Netherlands and the European Union, sustainability goals regarding the reduction of carbon emissions and the increase of the share of renewable energy, are ambitious. The Dutch government aims to reduce carbon emissions in 2030[1] by 55% and is on course to reach anywhere between 44% and 52% [1]. In 2030 75% of all electricity in the Netherlands will be produced by renewable energy sources. Two things should be noted: 1) this is lower than the 85% goal and 2) electricity is only a part of all energy used. Looking at all energy, the European goal of 39% reduction by 2030 will probably not be reached, as current estimates show the Netherlands to reach anywhere between 30% and 37% [1].

Government programs and laws help reach the Dutch sustainability goals, by motivating and urging companies. Because of this companies are increasingly adapting sustainability goals as crucial parts of their strategies. Some companies, like GVB, go even further than the legal requirements. Instead of becoming emission-free by 2030, they moved their goal to 2025 [2]. Amongst others, the GVB has aimed to reach this by focusing on circularity of materials, energy savings in the infrastructure and investing in solar power. For example, recuperation of 15% of brake energy of metro trains can be used to charge the fleet of electric buses [3] and will be implemented in 2025 [4]. Also, in 2020, 5000 solar panels were placed on metro station roofs throughout the city. Both of these measures can help reduce grid congestion, which is becoming an increasingly major problem in the Netherlands.

In the Netherlands where space is generally limited and in strong competition, and NIMBY's contest proximity to renewable energy sources, unconventional solutions ought to be used to reach the country's sustainable energy goals. Committing to integrated photovoltaics, like building or vehicle integrated photovoltaics (BIPV and VIPV), can prove useful to reach multiple goals at once:
1) increasing the share of renewable energy production,
2) reducing grid congestion by consuming energy at the source and
3) novel and clever use of available space in the built environment.

1.2. Aim and Research Objectives

In this project, the PV potential of wagon surfaces of the Amsterdam metro network will be modeled and analyzed. The project aims to answer multiple questions:

- How could metro wagons be covered in PV modules and which challenges arise when doing so?
- Would this result in enough energy to account for the entire metro network, and if not, what part?
- Which alterations to the metro power network infrastructure are needed to this end?

When the model to find the PV potential of the metro network is finished, its results can be used to find the percentage of energy consumption of the metro network that can be compensated by wagon

[1] with respect to levels in 1990

integration of PV. The effect of the aboveground percentage of the metro network on the results is investigated too.

- Given that the Amsterdam metro network is$\sim$ 80% aboveground and that metro networks are usually underground, how would the energy yield and power series change for networks with different aboveground percentages?

The past research from TU Delft about PV integration in dynamic rather than static systems revealed specific probability distribution for the PV power of a fleet of vehicles. Therefore, another possible path for the research is to explore the probability distribution curve of PV power production on top of trains.

The intended outcomes of the research are

1. the PV power series and annual energy yield of a PV-covered Amsterdam metro fleet
2. the percentage of energy consumption of metro that can be compensated by wagon integration of PV and its dependence on the aboveground percentage
3. a probability distribution of the PV energy yield

1.3. Report outline

In Chapter 2, the literature review performed for this research will be discussed. In addition, the conceptual basis of relevant topics will be explained. In Chapter 3, the method to find the answers to the research questions in Section 1.2 will be explained. It provides the framework of the simulation model used. In Chapter 4 the results of the simulation model are provided. These results are then discussed in 5 as well as recommendations for further and future research using a similar approach. In Chapter 6, the conclusion to the research questions will be provided.

2

Theory

2.1. PV energy

Photovoltaic (PV) technologies convert energy from sunlight into electrical energy. These technologies offer numerous advantages with respect to conventional, fossil-based energy technologies. PV knows zero emissions during operation, low operational costs and PV can be used in decentralized systems [5]. In 2024, according to the International Energy Agency (IEA), PV energy production accounted for 6.8% of global electricity production [6]. The IEA projects PV to overtake wind in 2027 and hydropower in 2029. The latter is impressive as hydropower has traditionally been the most prevalent renewable energy source. See Figure 2.1.

2.1.1. PV cells

A PV cell is the smallest unit of a PV module. The element that generates electricity is a p-n junction semiconductor that generates a photocurrent when exposed to sunlight. There are various materials and technologies present in the PV market, each with their own characteristics regarding efficiencies and costs. The most common is crystalline silicon (c-Si) with a typical efficiency of $\sim$20% [5]. Thin-film cells, made of for example a-Si, CdTe and CIGS, have the benefit of being lightweight and flexible, but this comes at the cost of them generally having a lower efficiency than c-Si cells [5]. They have efficiencies ranging from $\sim 10 - 15\%$. They could be inexpensive, but due to c-Si's maturity in the market, the latter is currently more inexpensive [5]. Perovskites and multi-junction cells have the highest efficiencies, exceeding 30%, but are not commercially viable and are thus only used in niche applications.

The performance of a PV cell is determined by its J-V characteristic, where J denotes the current density and V the voltage. Under illumination, an ideal PV cell can be modeled by Equation 2.1 [5]. This equation describes the current density as the sum of three terms. These terms concern the dark diode current density, the effects of the series and shun resistances on the current density and the photo generated current density respectively.

$$J = J_0 \left[\exp\Big(\frac{q\,(V + AJR_s)}{nkT} \Big) - 1 \right] + \frac{V + AJR_s}{R_{sh}} - J_{ph} \tag{2.1}$$

where J_0 is the diode saturation current, q the elementary charge, A the cell area, k Boltzmann's constant, T the cell temperature, n the diode ideality factor, R_s and R_{sh} the series and shunt resistances of the cell and J_{ph} the photo-generated current.

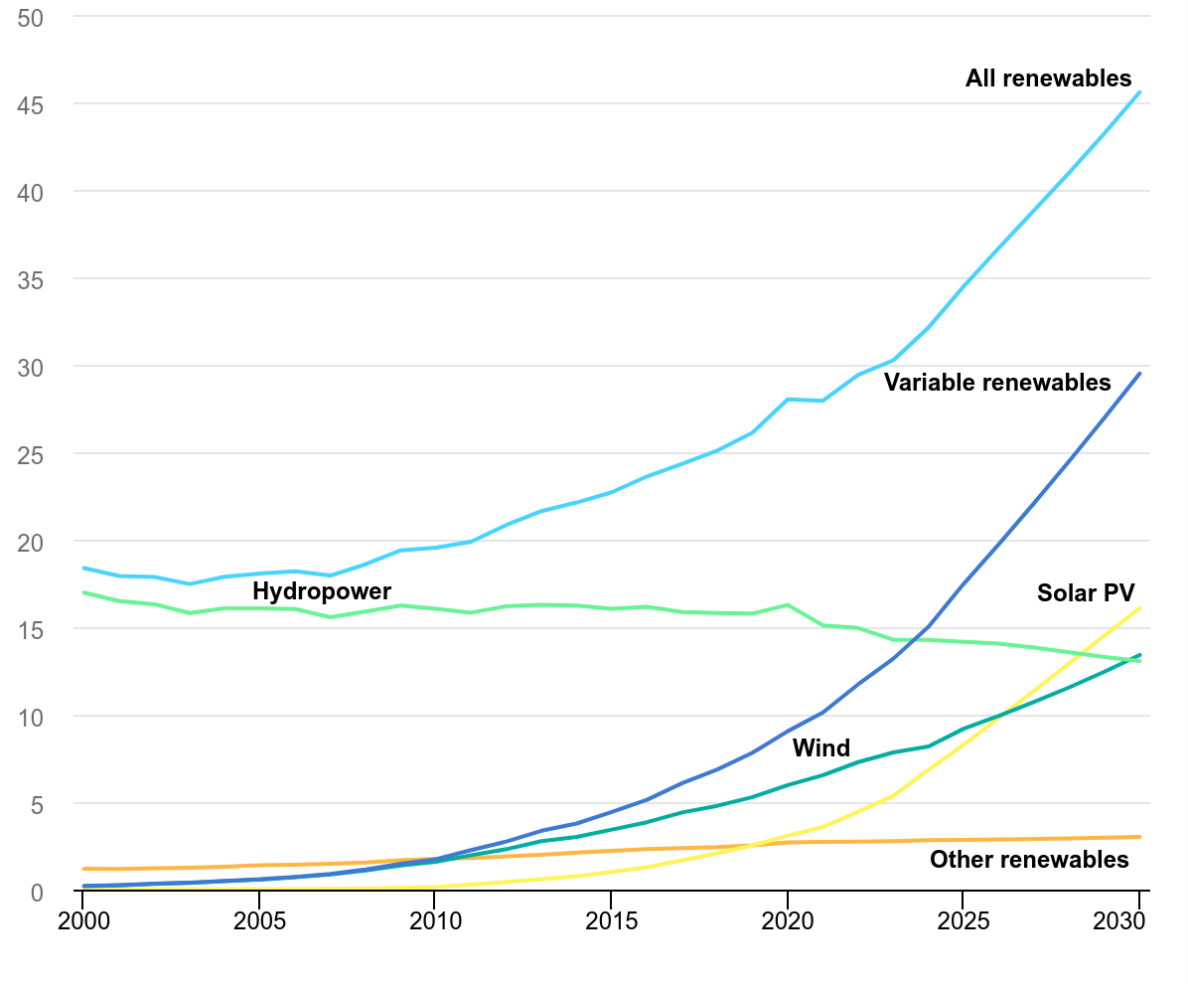

Figure 2.1: Shares of renewable electricity generation by technology in the global electricity generation from 2000 to 2030 [6].

From this expression, important PV cell characteristics can be derived. The open-circuit voltage (V_{OC}) is the voltage when there is no net current:

$$V_{OC} = \frac{k_B T}{q} ln\left(\frac{J_{ph}}{J_0} + 1\right) \approx \frac{k_B T}{q} \ln\left(\frac{I_{\text{ph}}}{I_0}\right) \tag{2.2}$$

The short-circuit current density (J_{SC}) is the current density when there no voltage. If it is assumed $R_S \approx 0$ then

$$J_{SC} \approx J_{ph} \tag{2.3}$$

The fill factor (FF) is the ratio between the maximum power point (P_{MPP}) and the product of J_{SC} and V_{OC}. It is a useful metric to characterize the J-V curve and is influenced by the R_s and R_p [5].

$$FF = \frac{V_{MPP} J_{MPP}}{V_{OC} J_{SC}} \tag{2.4}$$

The efficiency (η) is the ratio between the produced electrical power and the power from the incident light.

$$\eta = \frac{P_{out}}{P_{in}} = \frac{J_{MPP} V_{MPP}}{P_{in}} = \frac{V_{OC} J_{SC} FF}{P_{in}} \tag{2.5}$$

For single-junction c-Si cells, the efficiencies that can be reached in lab settings is approaching the theoretical Shockley–Queisser limit of about 33% [5].

2.1.2. PV modules

In practical applications, individual PV cells are connected in series and parallel configurations to form PV modules [5]. A PV module consists of many cells in series where each cell in series adds to the overall voltage. Strings of PV cells placed parallel result in a higher overall current. Bypass diodes can be used across strings of cells in order to mitigate the effects of partial shading. When even a small portion of a series string is shadowed, as the resistance of the shadowed cell increases, the current through the entire string is reduced. This can lead to hot-spots and power loss. Bypass diodes provide alternate current paths, allowing the unshaded cells to continue contributing power.

Integrated PV modules may require specific technologies in order to work optimally. For example, bypass diodes can increase the resilience of modules to partial shading, which is especially relevant for integrated, dynamic PV systems [7]. Thin-film materials, being flexible and lightweight, are ideal for use with curved surfaces and weight-sensitive applications [8].

2.1.3. PV systems

A PV system comprises of PV modules connected to a type of load as well as electronics that enable power conversion and energy storage. The type of electronics used depends on the configuration and use of the PV system. See Figure 2.2 for schematic examples of simple stand alone and grid connected PV systems. These PV system elements are referred to as the balance-of-system (BoS). In a typical grid-connected system, the output of the PV array is connected to the grid via a DC/AC inverter. On the other hand, for stand-alone applications, DC/DC converters are used in conjunction with battery storage to provide a stable power supply. Regardless of the configuration, a maximum power point tracker (MPPT) is essential to have the system deliver the maximum power. As the environmental conditions change continuously, so too would the output power without an MPPT. An MPPT continuously adjusts the operating voltage and is incorporated in the inverter or converter [5]. Common MPPT algorithms include perturb-and-observe and incremental conductance methods, which are simple and robust, as well as more advanced techniques employing for example machine learning[9].

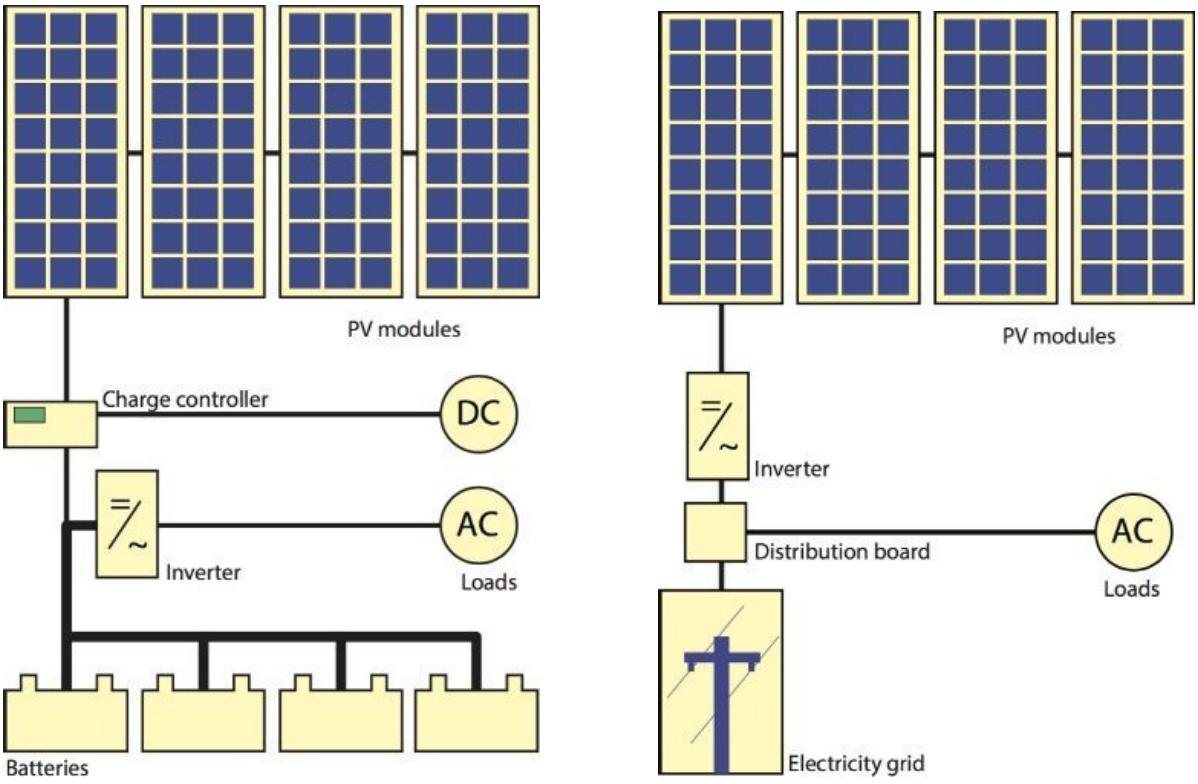

Figure 2.2: Examples of a stand-alone (left) and grid-connected (right) PV system [5].

The performance of PV systems is influenced by many factors. For static installations, system yield can be modeled using historical weather data and known module performance parameters. On the other hand, dynamic applications require dynamic analysis of how orientation and shading change over time. Nonetheless, the fundamental components of generation (PV array) and conditioning (power converters with MPPT, plus possibly storage) remain the same: the system is still a PV array with power converters with integrated MPPT.

Depending on the design of the PV system and its control, they can range from small-scale applications of a few watts to utility-scale installations in the order of megawatts.

2.2. Integrated PV technologies

Rather than mounting PV modules on dedicated structures, PV technologies can also be integrated into existing surfaces. Both building-integrated and vehicle-integrated photovoltaics, BIPV and VIPV respectively, are well-known examples. The generated power can then be used to cover a part of the energy demand of the building or vehicle. By utilizing these otherwise unused surface areas, integrated PV can reduce the effective land footprint of PV and enable power generation directly where it is consumed.

2.2.1. Vehicle integrated PV technologies

Vehicle-integrated PV (VIPV) has gained attention in recent years as improvements in solar cell efficiency and cost make on-vehicle generation more feasible. The potential benefits of VIPV include extended driving range or reduced fuel consumption for hybrid, solar-assisted electric vehicles[10]. They also contribute to the overall lowering of greenhouse gas emissions of the transportation sector [11]. Several pilot projects and prototypes have demonstrated VIPV in practice. For instance, the Byron Bay solar train in Australia is a commuter train retrofitted with 128 thin-film PV modules with a rated power of 50 W each [12]. Another example is Indian Railways which instead used c-Si modules with a rated power of 300 W each [11]. These successful implementations proved that PV can function reliably in the vibration and movement environment of vehicles.

A study by Vasisht *et al.* [13] on VIPV for Indian Railways, showed that a single PV-covered wagon could generate at least $\sim$18 kWh of electricity per day. This could save 1700 liters of diesel annually. This translates to a significant reduction in operating costs and emissions. A later case study by Darvishpour *et al.* [11] analyzed PV integration on an electric train in Milan's regional railway. Using a computer model, they found that PV modules on a train roof could supply up to nearly 10% of its auxiliary power consumption, yielding about 600 MWh of energy per year and reducing CO_2 emissions by over 27 tons annually [11]. These figures underscore that, even though the fraction of a vehicle's total energy demand covered by PV is limited by the available area, the absolute energy and fuel savings over time can be substantial.

For road vehicles, the integration of PV has mostly been explored on electric cars and buses. Hoth *et al.* [10] assessed the solar energy potential for passenger cars with integrated PV in Berlin. Their analysis of tens of thousands of parking locations showed that an average PV-equipped electric car could gain an extra 7-14 km of driving range per day, corresponding to roughly 2500 km of additional range per year [10]. While this represents only a portion of a vehicle's daily usage, it can reduce grid charging and thus relief stress on that system.

Implementing PV on vehicles presents unique technical challenges. Vehicle surfaces are often curved, requiring flexible or custom-shaped PV modules [8]. The operating conditions include constant vibrations, a wide range of temperatures, and exposure to wind loads. Unlike stationary panels which can be optimally tilted, VIPV is constrained to the vehicle's geometry. As a result, the incident irradiance can be sub-optimal and varies with the vehicle's orientation. Shading is another critical issue: moving vehicles experience shadows from their changing surroundings. Examples are bridges, tunnels, other vehicles and, in the case of electrified rail, from wires and poles. Macías *et al.* [7] highlight that partial shading can lead to significant drops in energy output. Their model, using realistic shading profiles, showed that for different interconnection configurations, the difference in energy output could be as large as 41%. They show that clever design of these interconnections can mitigate these losses [7].

2.3. PV system modeling

PV system models allow to predict how much energy a PV installation will generate under varying conditions and to identify any design optimizations needed for maximum yield. A PV system model takes into account all levels of the system: from the electrical characteristics of individual cells and modules, to the environmental irradiance conditions and even up to the system-level energy flow including power electronics and storage.

At the cell level, Equation 2.1 is widely used to represent the J–V curve of a PV device [5]. The parameters for this model can generally be obtained from manufacturer datasheets. For modeling a full PV module or array, the cell model is scaled and extended to include series/parallel connections and the effect of bypass diodes.

In a conventional PV system study, historical irradiance and temperature data are used to compute expected energy production for a fixed location. In the case of a metro wagon with PV panels, the location is not fixed. The model must trace the train's route, orientation, and any shading obstacles over time. This has led researchers to adopt advanced tools such as geographic information system (GIS) models and 3D city models to simulate the solar irradiance on moving vehicles [10][7]. For instance, Hoth *et al.* [10] utilized digital surface models of an urban environment to determine how buildings and trees shade a car at various parking spots and times of day. Similarly, for a train route, one could map the track and surrounding structures to compute solar exposure as a function of distance along the line [7]. Chen *et al.* [14] used a GIS-based approach to evaluate PV potential along an entire high-speed rail corridor, integrating over distance and time to estimate total energy generation.

To accurately model the irradiance input to the PV modules, it is necessary to decompose the total irradiance into direct, diffuse, and ground-reflected components. Each component must then be projected onto the inclined surface of the module. This involves computing geometric relationships such as the angle of incidence (AOI), shading factor (SF), and sky view factor (SVF), which account for obstruction, orientation, and exposure. The equations below describe this decomposition [5]:

$$G_M = G_{dir} + G_{dif} + G_{ground} \tag{2.6}$$

Here, G_M denotes the total irradiance incident on the module. It is the sum of the direct component (G_{dir}), the diffuse component (G_{dif}), and the ground-reflected component (G_{ground}).

$$G_{dir} = DNI \cdot \cos(AOI) \cdot SF \tag{2.7}$$

$$\cos(AOI) = \sin(\theta_m)\cos(\alpha_s) + \cos(A_m - A_s) + \cos(\theta_m)\sin(\alpha_s) \tag{2.8}$$

The direct component is determined by:

- DNI: direct normal irradiance,
- AOI: angle of incidence between the Sun's altitude angle and the module normal,
- SF: shading factor,which is 1 if the Sun is visible, 0 if obstructed.

The angle of incidence is computed based on the module tilt angle θ_m, the solar altitude α_s, and the azimuthal difference between the module orientation A_m and the solar azimuth A_s.

$$G_{dif} = G_{iso} + G_{cir} + G_{hor} \tag{2.9}$$

$$G_{iso} = DHI \cdot SVF \cdot (1 - F1) \tag{2.10}$$

$$G_{cir} = DHI \cdot F1 \cdot \left(\frac{A}{B}\right) \cdot SF \tag{2.11}$$

$$G_{hor} = DHI \cdot F2 \cdot \sin(\theta_m) \tag{2.12}$$

The diffuse component consists of three parts:

- G_{iso}: isotropic component, modeling the sky as uniformly bright,
- G_{cir}: circumsolar component, modeling increased brightness near the sun,
- G_{hor}: horizontal brightening component, modeling increased brightness near the horizon.

These are computed using:

- DHI: diffuse horizontal irradiance,
- SVF: sky view factor,
- $F1$, $F2$: Perez coefficients (see Appendix E),
- $A = \max(0, \cos(AOI))$,
- $B = \max(\cos(85°), \sin(\alpha_s))$.

$$G_{ground} = GHI \cdot \alpha_{albedo} \cdot (1 - SVF) \tag{2.13}$$

The ground-reflected component is calculated from:

- GHI: global horizontal irradiance,
- α_{albedo}: albedo coefficient, representing the ground reflectivity,
- $1 - SVF$: the fraction of the ground visible to the module.

Another layer of PV system modeling involves the BoS components, particularly the power electronics and energy management. The inclusion of an MPPT algorithm in simulations can notably impact the predicted performance under fast-changing conditions, like a train driving underneath a viaduct. The model should incorporate the behavior of the DC/DC converters or inverters that implement MPPT. Conventional algorithms generally track the global maximum power point unless shading causes multiple peaks, in which case they might momentarily lock on a local peak.

The effects of temperature are also important in PV modeling. A higher cell temperature, leads to a lower efficiency of PV modules. Modeling the thermal behavior accurately is thus important for estimating the system yield. On a moving vehicle, increased air flow improves convective cooling of panels compared to stationary installations. The temperature coefficients, κ, used in models are generally provided on the datasheets of manufacturers. Typical values depend on the specific PV technology, but for c-Si this is about 0.4–0.5% per °C. Equation 2.14 describes the effect of temperature and irradiance on the efficiency [5].

.

$$\eta(T_M, G_M) = \eta(25°C, G_M)\,[1 + \kappa(T_M - 25°C)] \tag{2.14}$$

The effects of irradiance on $\eta(25°C, G_M)$ are described by Equations 2.15 to 2.19. In these equations, n represents the ideality factor of 1.2, k_B the Boltzmann constant and q the elementary charge.

$$\eta(25°C, G_M) = \frac{P_{MPP}(25°C, G_M)}{G_M \cdot A_M} \tag{2.15}$$

$$P_{MPP}(25°C, G_M) = FF \cdot V_{oc}(25°C, G_M) \cdot I_{sc}(25°C, G_M) \tag{2.16}$$

$$V_{oc}(25°C, G_M) = V_{oc}(\text{STC}) + \frac{nk_BT_{STC}}{q} \ln\left(\frac{G_M}{1000}\right) \tag{2.17}$$

$$I_{sc}(25°C, G_M) = I_{sc}(\mathsf{STC}) \cdot \frac{G_M}{1000} \tag{2.18}$$

$$FF = \frac{P_{mpp}}{V_{oc_{STC}} \cdot I_{sc_{STC}}} \tag{2.19}$$

3

Model

3.1. Overview

This chapter describes the model developed for the purpose of this research. The model was made in MATLAB and is designed to estimate the potential energy yield of PV modules mounted on metro trains. The model simulates the photovoltaic energy production during 2023. It accounts for many different factors, but most importantly for metro train position, skyline obstructions, temperature, irradiance, and system parameters. The result is a time-dependent and location-specific PV power production.
The chapter is structured as follows:

- Section 3.2 outlines the relevant physical and operational characteristics of the Amsterdam metro network.
- Section 3.3 details the input data used for simulation, including LiDAR data, climate data, PV specifications, and metro train timetables.
- Section 3.4 presents the different sub-models, each representing a specific aspect affecting PV generation, such as the skyline, the metro train position, the weather conditions, and module temperature.

3.2. Amsterdam Metro Network

The Amsterdam metro network is operated by GVB. It consists of 5 lines covering 39 stations and in 2023 GVB operated a total of 88 metro trains [15]. A map of the Amsterdam metro network, its lines and its stations can be seen in Figure 3.1. Table 3.1 summarizes information about the metro network: the line names, their start and end stations, the amount of stations per line, as well as their length and the percentage of length that is aboveground. For example, for line 52, the underground section is taken to be 6.5 km long and starts at Noorderpark station and ends right before station Zuid. For lines 51, 53 and 54, the tunnel is taken to be 3.5 km long and starts a little bit after station Amstel. See Figure 3.3. The choice for start and end stations is arbitrary as the trains run equally in both directions; the GVB does not seem to communicate a strict definition. For the purpose of this research it is however relevant to choose a convention, as the distinction between outbound and inbound trains is relevant in the model code. The chosen convention of start and end stations is summarized in Table 3.1. A metro train is outbound if it moves from start to end station and inbound if it moves from end to start station. To give an example,looking at both Figure 3.1 and Table 3.1, a line 50 train scheduled to depart from station Lelylaan in the direction of Gein station, will be considered outbound.

Line	Start station	End station	Stations	Length	% Above-ground	Duration
50	Isolatorweg	Gein	20	20.5 km	100%	40 min
51	Isolatorweg	Centraal Station	19	18.7 km	81%	35 min
52	Noord	Zuid	8	9.7 km	33%	15 min
53	Gaasperplas	Centraal Station	14	11.7 km	70%	22 min
54	Gein	Centraal Station	15	12.7 km	72%	24 min

Table 3.1: Summary of facts about the Amsterdam metro network.
Data on line lengths is based on Wikipedia (uncited); tunnel sections are measured visually using `freemaptools.com`.

The frequency of and the amount of trains on each line depend on the time of day, the day of the week and the time of year. The model does not take into account maintenance and delays. On weekdays there are more trains running per hour than on the weekends. During the summer period, generally a 6 week period between the start of July and the end of August, there are less trains running per hour than outside of this period. During the day there is a distinction in frequencies for various time intervals that could be categorized as off-peak hours, peak-hours, day-hours and evening-hours. These are summarized in Table 3.2.

Line	Before 07:00	07:00–09:00[a,b]	09:00–16:00[a]	16:00–18:30[a,b]	18:30–20:00	After 20:00
50	4	6	6	6	5	4
51	4	6	6	6	5	4
52	8	8	8	8	8	8
53	4	6	6	6	5	4
54	4	6	6	6	5	4

Table 3.2: Frequencies of the 5 metro lines for various time intervals in trains per hour for 2023 [16].
[a] During weekends, these frequencies are lowered to 5 trains/hour (except for line 52, which remains unchanged).
[b] For line 52 only, frequencies during these peak hours were increased to 12 trains/hour in 2024.

3.2.1. GVB Metro Trains

There are three types of trains in use on the GVB metro network: the S3/M4, M5 and M7. M5 is designed by Alstom from France and M7 by CAF from Spain . Little information about the dimensions of the various types of trains is publicly available, so estimations are made. Most of the numbers as well as the schematics used in Figure 3.9a were retrieved via correspondence with an employee of GVB. The dimensions that are known are the total lengths and width of the various trains, as well as the width reserved for a pathway for maintenance on M7 trains. The latter width is 35 cm and is assumed to be comparable for the M4 and M5 models as well. An M5 train consists of 6 wagons (or ”bakken” in Dutch) that are in total 120 m long, 3 m wide. An S3/M4 train consists of three units, being about 60 m long and 3 m wide. M7 trains can either be single trains or two coupled trains; the length then is either 60 m or 120 m. All trains have a height w.r.t. the track height of 3.8 m. Without access to the finer dimensions of the roof sections on the trains, the available area for PV integration is estimated by using the known width of 3 m and scale drawings of the M5 Alstom train (as in Figure 3.9a). To estimate the available areas for the other trains, the ratio of the available area to the total area of the M5 trains was used. The ratio for the other trains was assumed to be the same or at least similar to that of M5 trains.

When a train reaches an end station, the train starts running backwards. The driver gets out of the driver’s cabin and walks to the other end of the train to enter the driver’s cabin on that side. This means that PV modules installed on the port side in the outbound direction are the same modules as the starboard side panels in the inbound direction.

Except for Line 52 which only runs M5 trains, the other lines each run a mix of M4, M5 and M7. With help of a GVB document the distribution per line was approximated. This document was retrieved via correspondence with a GVB employee and is not publicly available. All calculations are performed

using parameters for the most common M5 trains. Since the fleet consists of smaller trains too, taking only M5 values would overestimate the module power production. A scaling factor w.r.t. M5 trains is needed. In order to do this, three factors need to be taken into account. First, the available roof area depends on the type of train. Second, each metro line runs a different mix of trains. Third, the amount of trains running on a line depends on the time of day. Clever manipulation leads to a scaling factor per line. Note that since line 52 only consists of M5 trains, the scaling factor should be 1. This scaling factor is then used to adjust the power output calculated for M5 trains to reflect the actual train composition per line.

First, make a vector containing the relative rooftop area's of all types of trains w.r.t. M5. From top to bottom these are M4, M5, M7a and M7b.

$$A_{relative} = \begin{bmatrix} 0.2575 \\ 1.0000 \\ 0.4967 \\ 0.9930 \end{bmatrix} \tag{3.1}$$

Second, make a matrix where the amount of rows is the amount of metro lines and the amount of columns is the amount of different trains. This matrix represents the mix of trains per line. In reality these trains do not all run simultaneously, so the assumption is made that they do. In order to keep the correct number of trains in subsequent calculations, the rows are normalized.

$$M_{line,type} = \begin{bmatrix} 2 & 6 & 1 & 0 \\ 3 & 4 & 3 & 1 \\ 0 & 8 & 0 & 0 \\ 2 & 5 & 3 & 2 \\ 2 & 5 & 3 & 2 \end{bmatrix} \tag{3.2}$$

Finally, the line-type matrix is row-normalized and multiplied by the relative area vector, resulting in a per-line scaling factor.

The amount of trains running simultaneously also depends on the time period, e.g. during rush hour or not. However, since the model calculates the yield for each timetable timestamp, this is automatically accounted for.

$$A_{scaled} = \hat{M}_{line,type} A_{relative} = \begin{bmatrix} 0.7791 \\ 0.6596 \\ 1.0000 \\ 0.7493 \\ 0.7493 \end{bmatrix} \tag{3.3}$$

3.3. Input data

3.3.1. LiDAR data

LiDAR data are used as input for the skyline model. LiDAR data used in this research is the Digital Surface Model (DSM) of the Actueel Hoogtebestand Nederland (AHN) available via PDOK. LiDAR is short for Light Detection And Ranging and is similar to the more commonly known radar, which in turn is short for Radio Detection and Ranging. Rather than radio waves, LiDAR uses laser pulses to determine the distance between the observer and investigated objects. This can be determined by knowing the speed of the laser pulse and measuring the time it takes for it to reflect off an object and return to the observer. With some additional information as well as some trigonometry, the height of the objects are estimated. The AHN has a spatial resolution of 0.5 m^2. Some precautions need to take place in order to be able to use the data. This is explained in Section 3.4.1.

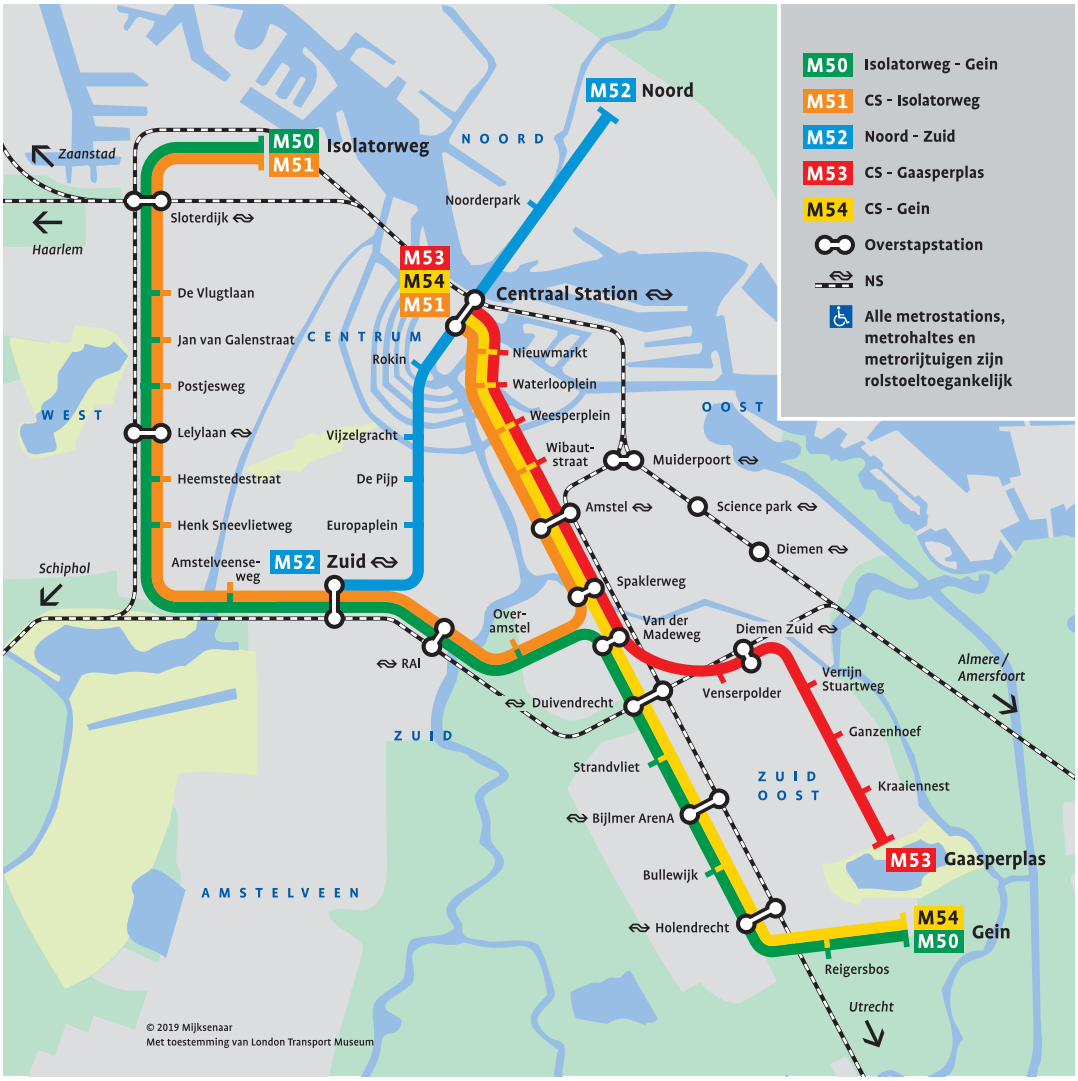

Figure 3.1: Map of the Amsterdam metro network showing its 5 lines as well as its 38 stations.

3.3.2. Climate data

Climate data is used both as an input for the weather model, the temperature model as well as the yield model. Climate data used in this research consists of the global irradiance and the ambient temperature for the KNMI weatherstation at Schiphol airport available via the open data portal of the KNMI.

The KNMI wind speed data contains some inconsistencies which became apparent when plotting the probability distributions. The wind speed is stored as a number with two decimals. Wind speed distribution is known to follow a Weibull distribution. For the probability distribution, the bins were defined so that each contained a number with two decimals. It was discovered that some bins did not contain any counts at all whereas others did. For example, at Schiphol 18Cm27 weatherstation during daylight hours in 2023, wind speeds of 4.71 m/s and 4.73 m/s did not occur, whereas 4.72 m/s and 4.74 m/s occurred 92 and 84 times respectively. This implies that there are some rounding errors occurring with the KNMI data collection. The plot showing this behaviour is shown in Chapter 4.2 in Figure 4.4. It was decided to inform to KNMI and keep the data for what it is, but use an amount of bins that is equal to the square root of the total amount of counts, as is common practice. The KNMI set out to investigate the results and found the reason for the missing bins. The KNMI was previously not aware and will perform future adjustments to the data collection accordingly. The full correspondence can be found in Appendix B.

3.3.3. Metro timetables

The timetables of the GVB metro network are used to approximate the positions of the metro trains. In total, ten timetables are used: two for each of the five metro lines, one in the outbound and one in the inbound direction. The timetables show the timestamps in HH:MM when a train leaves the corresponding station. There are different timetables for weekdays, Saturdays and Sundays. Additionally, the timetables differ slightly for different periods of the year. Examples of this are the less busy summer schedule and planned maintenance.

3.3.4. PV module parameters

PV module parameters are relevant for the temperature and yield models. In order to optimize the wagon roof coverage, it is assumed the GVB would commission custom PV modules. These modules are based on the LR4-60HPB-360M (see Appendix C), differing in size and related parameters. This type of PV panel is the same one as used by De Jong [17]. The maximum power and open circuit voltage both scale proportionally with the area.

3.4. Sub-models

3.4.1. Skyline model

The skyline model aims to output skyline profiles and consequently the SVF on the locations described by the metro line coordinates. A flowchart showing the in- and outputs and the various calculations performed in the skyline model is provided in Appendix D. Due to time constraints this was not done for the other sub-models.

A skyline profile shows the highest object in each direction as seen from the observer. In other words, it shows the angular altitude of surrounding objects as a function of their azimuth angle. An example is shown in Figure 3.2. This figure also shows the AHN map and the point from which the skyline is generated. Additionally, a photo was made from a point close by as a comparison.

The metro line coordinates for which the skyline profiles are calculated are retrieved from the Amsterdam municipality maps website. See Appedix A. This website provides open data for all sorts of mapping purposes, amongst others the coordinates of the GVB metro (and tram) lines. The dataset *TRAMMETRO_LIJNEN_2022* was used as it was up-to-date in 2023. This dataset is parsed and the coordinates of the metro lines are extracted. These coordinates are the location of the 'observer' in the skyline profile calculations. The locations of these metro line coordinates can be seen in Figure 3.3. There are 727 coordinates of which there are 455 not in a tunnel.

The heights of the surrounding objects of the metro lines are described in the Actueel Hoogtebestand Nederland. As described in Section 3.3.1, the AHN divides the mainland Netherlands into tiles. Only

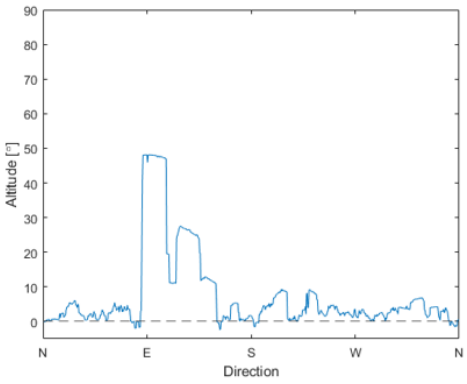

(a)

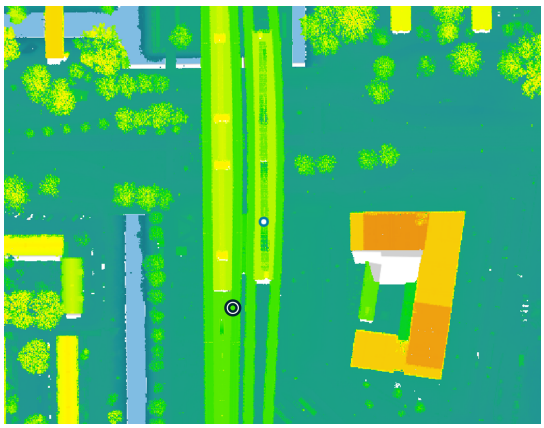

(b)

(c)

Figure 3.2:
(a) Skyline profile
(b) AHN map
(c) Photo taken

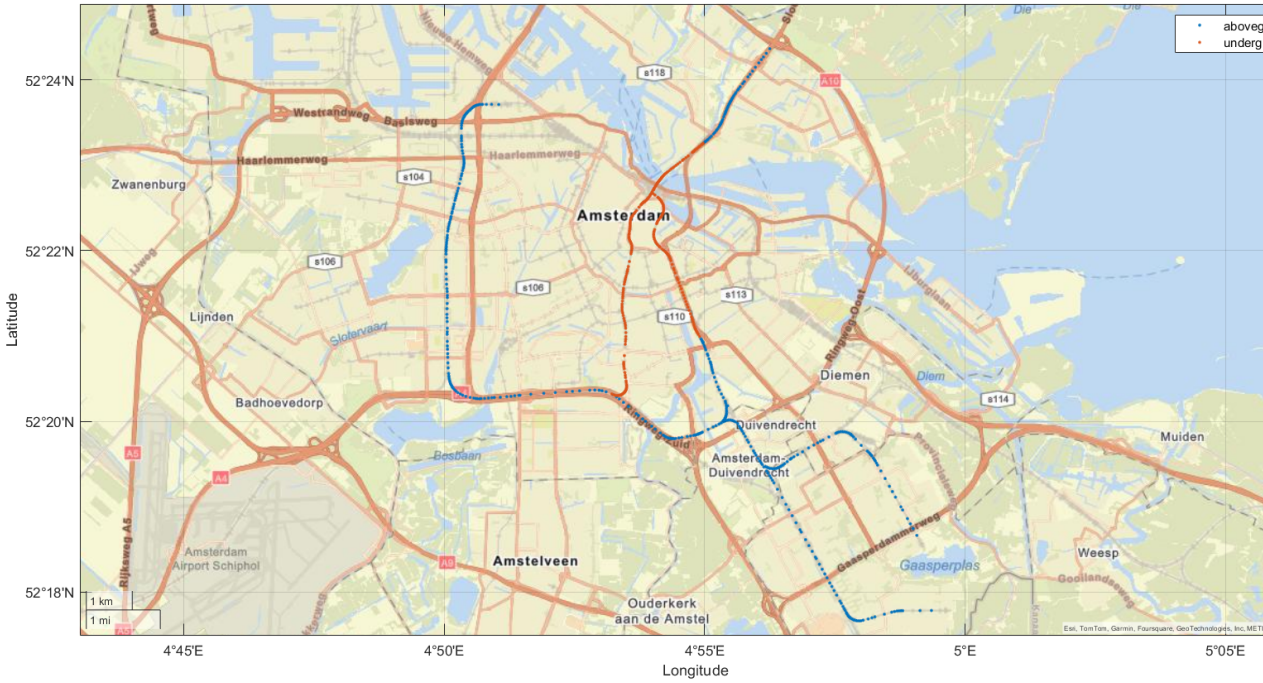

Figure 3.3: Map showing the locations of the metro line coordinates as well as if they are underground or aboveground.

the .tif files that contain the metro line coordinates are downloaded. In this research a scanning radius of 300 m around the observer is chosen. It should be noted that additional tiles may need to be downloaded dependent on the choice of scanning radius. The choice for scanning radius of 300 m was deemed by Ferri to be suitable for urban environments [18]; for larger scanning radii, the skylines would barely change whereas the computation time would increase more and more. For example, a common 5-story *portiekflat* is around $\sim 15m$ tall. At 300 m, the altitude angle of its roof as seen from an observer on ground level, would result in an altitude angle of 2.86°. This example does not even taken into account that the metro tracks themselves are generally raised in Amsterdam and that the modules are placed on top of the trains. Other, closer objects are more likely to show up.

There are however some flaws with the use of the AHN LiDAR data for this research. The metro line coordinates used, span each of the metro lines with a single line of points. There are multiple instances where the heights in the AHN dataset, misrepresent the actual track heights: viaducts, stations, artifacts and tunnel sections.

The metro lines consist of two parallel tracks, but the coordinates referring to them fall right in between these tracks. Since the AHN data has a spatial resolution of 0.5 m, and the distance between the two parallel tracks is larger than that, in some instances it happens that the metro line coordinate does not accurately represent the metro track height. This always happens with viaducts and stations. With viaducts the tracks are raised with respect to the ground below, but the metro line coordinate might correspond to a point on the ground below. The track height is thus misrepresented by the height difference between the track and the ground below. Without adjusting the height, the skyline would be generated from a point that would be too low. For stations, it is the other way around. With stations the metro line coordinate is a point on the station building. The track height again is thus misrepresented, this time by the height difference between the track and the station building roof. The skyline generated is from a point that is too high. Other instances where the height is misrepresented, are with LiDAR artifacts and tunnel sections. However, with these the misrepresentation is not due to the incorrect position of the coordinates. LiDAR artifacts in the DSM are objects that are not permanently there, but happened to be scanned when the plane flew by nonetheless. Prevalent examples are tower cranes as well as vehicles. There are instances that the metro line coordinates coincide with the location of a temporarily parked metro train. This can be seen in Figure 3.4b. Besides the artifact visually resembling a metro train, the height difference between the artifact and the metro tracks is 3.8 m, which is unsurprisingly the exact height of a metro train. For tunnel sections the height of the metro tracks is misrepresented, but there is no skyline generation for these points as the module irradiance will always be 0.

During manual inspection of all metro line coordinates and their heights in the AHN data, height differences are adjusted and saved in the *adjustedZ.mat* matrix. This matrix consists of 5 columns and as much rows as there are metro line coordinates, in this research 455. The 1st column contains the height difference that needs to be added to the height retrieved from the AHN data to reach the actual (manually inspected) track height. The 2nd column contains the manually inspected track heights. The 3rd, 4th, 5th columns contain binary information, categorizing the source of the misrepresentation. The 3rd column indicates stations, the 4th viaducts and artifacts and the 5th tunnel sections. For coordinates with correct representation, all columns contain 0's for that row. For coordinates referring to stations, the 3rd column contains a 1. With stations, a height adjustment up to the tracks by subtracting the height difference from the metro line coordinate height, would result in a skyline being generated from 'inside' of the station building. A zero height difference was chosen for these points, in order to still be able to generate a skyline, albeit slightly overestimated: less sky would be covered by buildings. For coordinates referring to viaducts or artifacts, the 4th column contains a 1. The height difference in the 1st column is positive for viaducts and negative for artifacts. For coordinates referring to tunnel sections, the 5th column contains a 1. This information is saved so that a module irradiance of 0 can be modeled for these instances. It should be noted that there are many instances where the metro line coordinates slightly misrepresent the track heights, even outside the scope of viaducts, stations, artifacts and tunnel sections. For these points, the height difference was taken into account only if it was found to be larger than 0.5 m. Smaller difference are too hard to account for with the manual visual inspection and would not impact the generated skyline significantly.

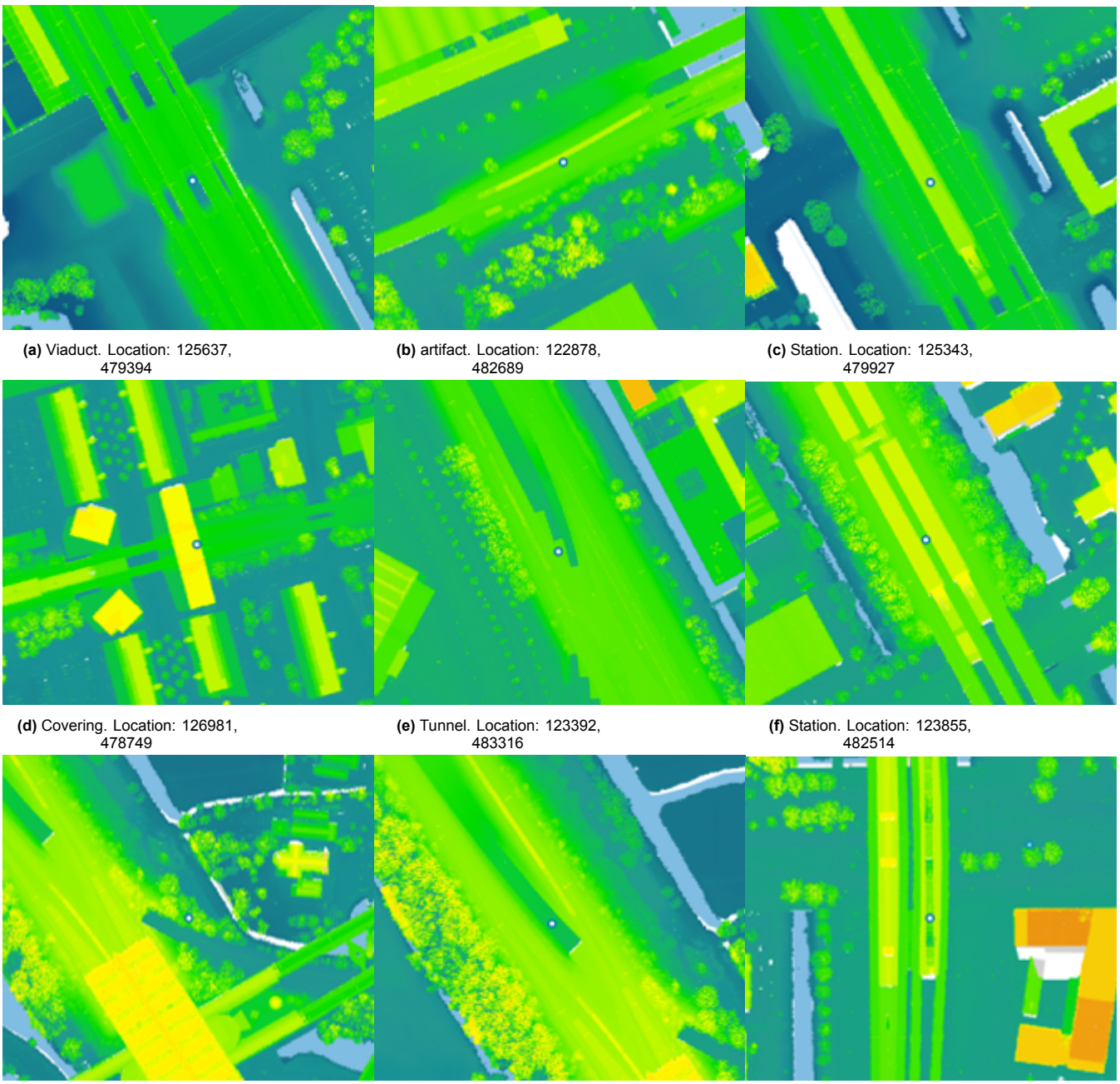

(a) Viaduct. Location: 125637, 479394

(b) artifact. Location: 122878, 482689

(c) Station. Location: 125343, 479927

(d) Covering. Location: 126981, 478749

(e) Tunnel. Location: 123392, 483316

(f) Station. Location: 123855, 482514

(g) Trees. Location: 124278, 481919

(h) Multiple tracks. Location: 124178, 481982

(i) Glass roof. Location: 117339, 485655

Figure 3.4: Various instances of misrepresentations of the metro track height. The specific misrepresentation origins are named below each image. The RD coordinates of the specific metro lines points, represented by the blue dots in each image, are also mentioned below each image.

Close-wall correction

Close-wall correction as described by Keijzer [19] is used to remove spikes from skyline profiles. A wall, that in reality is continuous, is a line of separated points in the AHN dataset. If this wall is close to the observer, the angle between those points may be smaller than the scanning angle, in this model 0.5$\circ$. The skyline scanner would then pick up a point behind the wall that is lower than the wall and create a dip in the wall. The close-wall correction algorithm is able to recognize these cases and discard them as outliers, replacing them with the same altitude angle as the wall.

3.4.2. Metro position model

The timetable is used to determine the position of the metro trains. Different parts of the train are in different positions and will experience different SVF's and SF's. To this end, the metro train is modeled as having three sections, the front, the middle and the back. The position of each section is the center. If a train is known to leave at a station at certain timestamp, the location of this station is then the position of the middle section of the metro train. The track in between two stations is divided into lengths that correspond to 1-minute time intervals[1]. This models the trains as standing still on those nodes for 1-minute before teleporting to the next node and standing there for 1-minute and so on. The nodes on the track that divide the track into 1-minute intervals, correspond to the position of the middle section of the metro trains. The positions of the front and back sections are linearly interpolated based on the position of the surrounding nodes and the length of the train. The positions of the front, middle and back sections are matched to the closest position of the 727 points.
Additionally, a distinction is also being made between the direction of the different train sections. On straight track sections these will be equal for the different metro train sections, but around curves these differ by a couple degrees.

3.4.3. Weather model

Data from the Royal Netherlands Meteorological Institute (KNMI) has been used for weather modelling. The solar irradiance, ambient temperature, cloud cover and wind speeds are relevant for the energy yield of a PV system. The KNMI data is open data and can be accessed via their API. A MATLAB code was written for this purpose.

The datasets are provided per month of the year and in 10 minute intervals. There are some faulty datapoints, appearing as NaN in MATLAB. Ideally, these would be replaced with neighbouring values as they should be similar. However, as faulty datapoints turn out to often cluster, this is not feasible. Instead, values of 0 have been chosen for GHI, okta, ambient temperature and wind direction. For wind speeds 0.01 was chosen, as the temperature model does not work with wind speeds of 0. When GHI is 0, it is as if the train is driving through a shaded section. For timestamps with faulty datapoints, output power will be 0, but the model will still update the module temperature and efficiency.

The solar irradiance datasets contain the Global Horizontal Irradiance (GHI) in W/m^2 in 10-min intervals for an entire year for all the weather stations on Dutch soil. The weather stations are characterized by their WGS84 coordinates as well as their height w.r.t. sea level.

A map of mainland Netherlands showing its KNMI stations is shown in Figure 3.5. The KNMI stations at the overseas special municipalities of Saba, St. Eustatius and Bonaire are not relevant for this research. The closest KNMI station to Amsterdam is located at Schiphol Airport.

The weather station used is the one at Schiphol. Dependent on the investigated variable, the location code differs slightly, but the latitude, longitude and altitude are in fact the same. The latitude is 52.31722 degrees and the longitude 4.789722. The altitude is -3.3 m. For the solar irradiance data, location Schiphol 18Ct is used. For temperature, Schiphol 18Cm27. For cloud cover, Schiphol 27t. For wind speed, Schiphol 18Cm27.

3.4.4. Temperature model

There are three forms of heat exchange between a PV module and its environment: radiation, convection and conduction. There are two possible ways to install the PV modules on the trains. One way

[1] This choice is technically inaccurate as it introduces some assumptions. For example, the speed of the train is now dependent on the amount of 1-minute time intervals between two stations in the timetable. However, as speed only affects wind-induced cooling in the temperature model, whose effect is marginal at best, this was deemed acceptable for the purpose of the research.

Figure 3.5: A map of the KNMI stations in mainland Netherlands.

is to mount them on top of the trains with a certain offset and the other is to integrated them in the train roof. With the mounted case, conduction only occurs at the mounts and since this only involves a small area, the effect can be disregarded. Conversely, with the integrated case, a large area is subject to conduction. However, with the integrated case, no air flow at the back is possible thus convection at the back will be zero, whereas with a mounted PV module this will be nonzero. Both situation are shown in Figure 3.6. The situation specific equations are shown in Figure 3.6, the common ones by Equations 3.4 to 3.7.

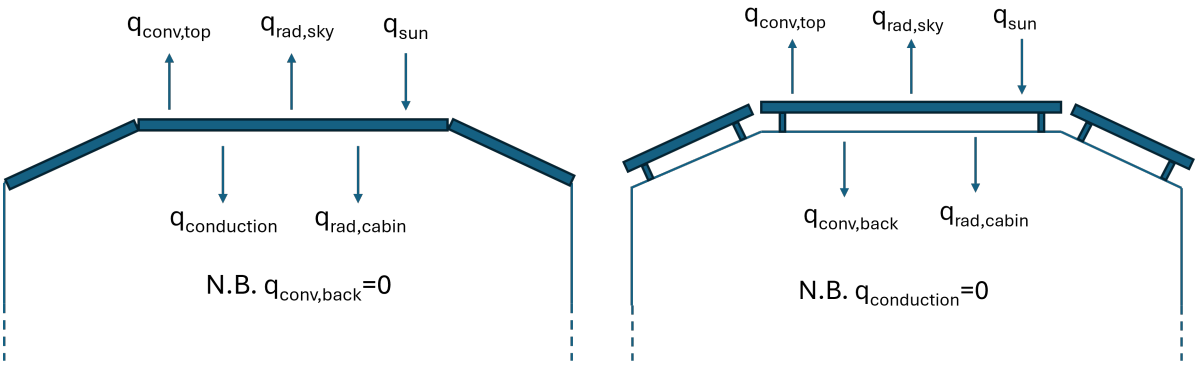

$$q_{sun} = q_{cond} + q_{conv,top} + q_{rad,sky} + q_{rad,cabin}$$
$$q_{cond} = h_{cd}(T_M - T_{cabin})$$

(a)

$$q_{sun} = q_{conv,back} + q_{conv,top} + q_{rad,sky} + q_{rad,cabin}$$
$$q_{conv,back} = h_{c,back}(T_M - T_{cabin})$$

(b)

Figure 3.6: Side by side comparison of the heat flux balance for (a) the integrated and (b) the stand-off case showing a cross-section of a metro train.

$$q_{sun} = \alpha G_M \tag{3.4}$$
$$q_{conv,top} = h_{c,top}(T_M - T_A) \tag{3.5}$$
$$q_{rad,sky} = h_{r,sky}(T_M - T_{sky}) \tag{3.6}$$
$$q_{rad,cabin} = h_{r,cabin}(T_M - T_{cabin}) \tag{3.7}$$

where q denotes heat flux, h heat transfer coefficients, α the absorptivity of the module and T the temperatures. The various subscripts denote whether they concern convective, conductive or radiative heat transfer and between which media.

For conduction losses, the thicknesses and thermal conductivities of the various layers are relevant. Little information is available on the internet, besides that the train roofs consist of aluminium and stainless steel [20]. In addition, a paper on PV modules on personal vehicles that discusses conduction losses is used to compare thicknesses and conductivities [21]. Tiano also mentions the use of an insulating mineral wool layer. The same layer will be considered for trains. The aluminium and stainless steel thicknesses will be taken as slightly larger: 3 mm and 5 mm respectively. Regardless of the choice of thickness of the metal layers, since the thermal conductivity of the insulating material is so small, it almost singlehandedly determines the values of the conductive heat transfer coefficient.

The Fuentes model results in an iterative expression for the module temperature. The code calculates the temperature according to the timetable of the trains (see Figure 3.7) per line and for both outbound and inbound trains. So it does this a total of 10 times. Any train that moves outbound and reaches the final station on the line, also will move inbound to the initial station. To correctly iterate the module temperature, one would have to carry over the final temperature of an outbound/inbound train and use it as the initial temperature of the corresponding inbound/outbound train. In this model however, it was chosen to use the final temperature of one outbound/inbound train as the initial temperature of the next outbound/inbound train. This effectively means the temperature is iterated for all columns in the

Lijn 50	Isolatorweg > Gein													Maandag t/m vrijdag | 16-09-2024 - 20-09-2024
Isolatorweg			05:48	06:03	06:18	06:33	06:48		07:03	07:18	07:28	07:38	07:48	07:58	08:08	08:18
Station Sloterdijk			05:51	06:06	06:21	06:36	06:51		07:06	07:21	07:31	07:41	07:51	08:01	08:11	08:21
Burg.de Vlugtlaan			05:52	06:07	06:22	06:37	06:52		07:07	07:22	07:32	07:42	07:52	08:02	08:12	08:22
Jan van Galenstraat			05:54	06:09	06:24	06:39	06:54		07:09	07:24	07:34	07:44	07:54	08:04	08:14	08:24
Postjesweg			05:56	06:11	06:26	06:41	06:56		07:11	07:26	07:36	07:46	07:56	08:06	08:16	08:26
Station Lelylaan			05:58	06:13	06:28	06:43	06:58		07:13	07:28	07:38	07:48	07:58	08:08	08:18	08:28
Heemstedestraat			05:59	06:14	06:29	06:44	06:59		07:14	07:29	07:39	07:49	07:59	08:09	08:19	08:29
Henk Sneevlietweg			06:00	06:15	06:30	06:45	07:00		07:15	07:30	07:40	07:50	08:00	08:10	08:20	08:30
Amstelveenseweg			06:03	06:18	06:33	06:48	07:03		07:18	07:33	07:44	07:54	08:04	08:14	08:24	08:34
Station Zuid			06:06	06:21	06:36	06:51	07:06		07:21	07:36	07:47	07:57	08:07	08:17	08:27	08:37
Station RAI			06:07	06:22	06:37	06:52	07:07		07:22	07:37	07:50	08:00	08:10	08:20	08:30	08:40
Overamstel			06:11	06:26	06:41	06:56	07:11		07:26	07:41	07:53	08:03	08:13	08:23	08:33	08:43
Van der Madeweg	05:48	06:03	06:13	06:28	06:43	06:58	07:13	07:26	07:28	07:43	07:56	08:06	08:16	08:26	08:36	08:46
Station Duivendrecht	05:50	06:05	06:15	06:30	06:45	07:00	07:15	07:27	07:30	07:45	07:57	08:07	08:17	08:27	08:37	08:47
Strandvliet	05:51	06:06	06:16	06:31	06:46	07:01	07:16	07:28	07:31	07:46	07:58	08:08	08:18	08:28	08:38	08:48
Station Bijlmer ArenA	05:53	06:08	06:18	06:33	06:48	07:03	07:18	07:30	07:33	07:48	08:00	08:10	08:20	08:30	08:40	08:50
Bullewijk	05:54	06:09	06:19	06:34	06:49	07:04	07:19	07:31	07:34	07:49	08:02	08:12	08:22	08:32	08:42	08:52
Station Holendrecht	05:56	06:11	06:21	06:36	06:51	07:06	07:21	07:34	07:36	07:51	08:04	08:14	08:24	08:34	08:44	08:54
Reigersbos	05:58	06:13	06:23	06:38	06:53	07:08	07:23	07:35	07:38	07:53	08:05	08:15	08:25	08:35	08:45	08:55
Gein	06:00	06:15	06:25	06:40	06:55	07:10	07:25	07:37	07:40	07:55	08:08	08:18	08:28	08:38	08:48	08:58

Figure 3.7: Timetable of Line 50 headed to Gein (outbound) valid from 16-09-2024 to 20-09-2024

timetable in order. This is a sound approximation since the trains run on the same track (just in the opposite direction) and experience more or less the same weather effects (they occur within an hour of each other).

The mounted case will experience a cooling effect by the convection heat loss at the back that it is more significant than the heat loss by the conduction loss at the back in the integrated case. This is an argument for installing the PV modules on a mount. However, as this may provide a higher yield in a computer model, in practice this will lead to problems. Debris may get stuck behind the modules which could lead to various problems and would be hard to clean. This is why only the integrated case is used within the model. By solving the system of equations consisting of Equations 3.4 to 3.7 as well as those in Figure 3.6a, the resulting module temperature can then be written as in Equation 3.8

$$T_M = \frac{\alpha G_M + h_{c,top} T_A + h_{r,sky} T_{sky} + (h_{cd} + h_{r,cabin}) T_{cabin}}{h_{c,top} + h_{cd} + h_{r,sky} + h_{r,cabin}} \tag{3.8}$$

Wind shear effects are generally used to scale wind speed values from anemometer measurements on certain heights to the heights of the module. In this research, these effects are disregarded. In order to include it, the heights of all possible metro positions need to be determined. As written in 3, the heights for all 456 skyline locations were determined manually. One would have to repeat that process for all interpolated coordinates, begging the question how significant the effects would be. The equation for wind shear is given by

$$w_M = w_0 \left(\frac{y_M}{y_0} \right)^{\alpha} \tag{3.9}$$

where w_M is the wind speed at module height, w_0 the wind speed at anemometer height, y_M the module height, y_0 the anemometer height and α the wind shear exponent which depends on the surrounding environment but is typically taken to be 0.25 in the built environment.

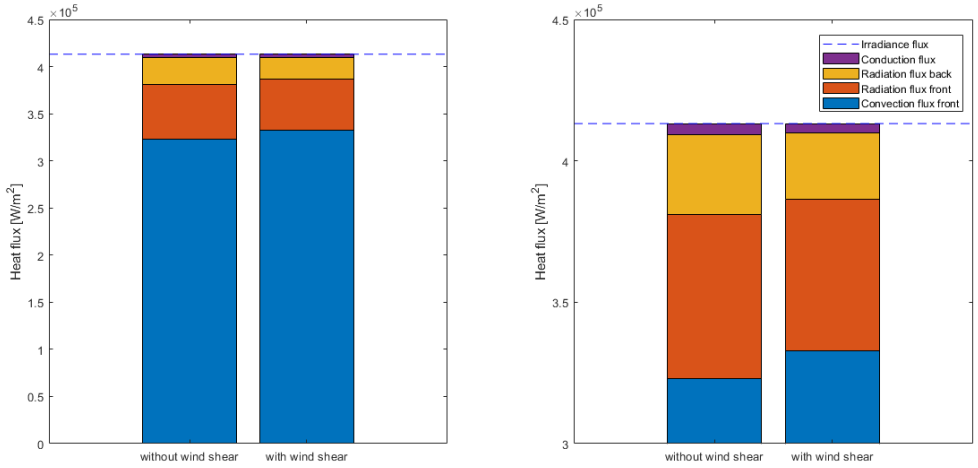

Figure 3.8: Comparison of heat flux components with and without the wind shear effect for the 1st of January 2023.

Consider the following example to investigate the significance of including wind shear. The height at which anemometers measure wind speed is generally 10 m with respect to the ground. At the Schiphol KNMI station, the ground height is -3.3 m, meaning the measuring height would be 6.7 m. At the viaduct close to the GVB "Logistiek Centrum Metro", a track height of 15 m is reached, meaning a module height of 18.8 m. Using Equation 3.9, this provides an increase in wind speed of 29.4 %. This seems significant, but as the wind speed is only relevant for the forced convection calculations in the temperature effects, the overall effect it has is less noticeable. This is illustrated in Figure 3.8, where all heat fluxes are compared with and without the effect of wind shear. This was done for the 1st of January with a constant wind shear effect of 29.4 %. In reality, the wind shear effect will generally be much lower, so this can be seen as a sort of upper bound. The share of the convection heat flux in all heat exchange increased from 78.2 % to 80.6%, so the difference in convection heat flux was only 3.1 %. The effect of wind shear is larger than the entire effect of conduction.

In the wind shear equation, the module height and the reference height are divided by one another. In the Netherlands, heights can be negative with respect to sea level. Without changes to the equation, this would lead to negative wind speeds, which are impossible. In order to remedy this, all heights are calculated with respect to the lowest point found encountered as track height, so as to have an absolute scale. This height is -5.3061 m and occurs at 52°23'16.1"N 4°54'59.8"E, which is the lowered track section leading into the IJ-tunnel from station Noorderpark.

A possible improvement to the temperature model (and the yield model as well) is the inclusion of the time spent at the end stations of each line. The vehicle speed would be zero and forced convection would be solely due to the ambient wind speed. The modules would heat up more than is the case in the current model, resulting in lower efficiencies and lower yield. One argument not to include the time at the end stations is the lack of irradiance at most of the end stations. Only Isolatorweg experiences full irradiance, whereas Gein en Gaasperplas are partially covered and Centraal Station and Noord are fully covered.

3.4.5. Yield model

For the calculation of the Sun's position in the sky, *solarPosCalculatorJD.m* was used. For a given timestamp, the azimuth and altitude of the Sun, does not vary significantly with location. For example, at January 1st at 8:51, taking the largest differences in longitude and latitude that occur in the location dataset, the maximum difference in azimuth and altitude are 0.1372 and 0.0166 degrees respectively. Both are lower than the resolution of 0.5 degrees used to determine SVF and SF. In order to reduce runtime, a central location was used, rather than using the current location at each timestamp. This location is 52°20'43.4"N 4°54'43.2"E.

In order to calculate the module irradiance, G_M, all of GHI, DHI and DNI are needed as per Equation 2.6.

The KNMI data only provides GHI so DHI and DNI have to be calculated with the help of a decomposition model. To this end, the BRL model was used. This model calculates the diffuse fraction (DHI/GHI) with the only inputs being GHI, location, time zone and time.This is done with the help of multiple predictor variables. The diffuse fraction is then used to calculate DHI and from there, DNI (Equation 3.10) [22].

$$DNI = \frac{GHI - DHI}{sin(solaraltitude)} \tag{3.10}$$

The BRL model only takes hourly GHI values as input and produces hourly DHI and DNI outputs. The GHI data from KNMI comes in 10 minute intervals and the module irradiance will be calculated in 1 minute intervals. In order to use the KNMI data as input for the BRL model, six consecutive data points need to be averaged. In this process, information is lost. In order to remedy this, a moving average is devised. This average works as follows. First, the hourly GHI average is calculated starting at XX:00, by taking its GHI value and the next 5 values and then averaging them. Secondly, the GHI average for XX:10 is calculated in the same way. And so on until XX:50, meaning it is performed six times. The BRL model is then used six times in succession to calculate DHI and DNI with hourly GHI data as inputs. The first DHI and DNI value corresponds to XX:00, the second one to XX:10 and so on until the sixth one, which corresponds to XX:50. Then these values are interpolated linearly to reduce the 10 minute intervals to 1 minute intervals.

The module irradiance is the sum of the direct, diffuse and reflected components. The reflected irradiance is calculated as in Equation 3.11. The reflected irradiance is all irradiance that is reflected from the surrounding ground and buildings. If you take all surroundings and you subtract the sky, you are left with the ground and the buildings, hence $1 - SVF$. It should be noted that there is no distinction in albedo between the ground and buildings; they are taken to be the same in this model.

$$G_{reflected} = GHI * \alpha * (1 - SVF) \tag{3.11}$$

3.4.6. Customized solar modules

Although each type of metro train has different roof dimensions, as described in Section 3.2.1, the optimization was only done for M5 trains. The total area on the other trains is just scaled w.r.t. M5, as described by Equation 3.1.

The roof of a bak consists of three sections: the flat part and the two slanted sections. These slanted sections happen to have a tilt of $\sim$30°, which is the optimal tilt of statically placed PV modules in the Netherlands. The relevant dimensions of these roof sections for finding the number of panels as well as their dimensions are found in Figure **??**. Finding the number of panels and their dimensions was an iterative process.

For the flat section, the panel is 1.17m x 0.74m, or $\sim 0.87m^2$. This would fit 40 modules on bak 1, 48 on bak 2 and another 40 on bak 3. For the slanted sections, the dimensions are 1.75m x 0.67m, or $\sim 1.17m^2$. This would fit 21 modules on bak 1, 22 on bak 2 and another 21 on bak 3.

A LR4-60HPB-360M has dimensions of 1.755m x 1.038m, or $\sim 1.82m^2$. Scaling its maximum power of 360 W with the areas of the flat and slanted roof sections, this results in $\sim 172W$ and $\sim 231W$ respectively. Using the number of panels for flat sections, the flat section of an M5 train has a maximum power of $2 * (40 + 48 + 40) * 172W =\sim 44kW$. Using the number of panels for slanted sections, each slanted section of an M5 train has a maximum power of $2 * (21 + 22 + 21) * 231W =\sim 30kW$

3.4.7. Storage method

Storing the data of all outputs, is a clever endeavor. An example of the storage method and its usage of cells is shown below for the module irradiance, G_M. Not all parameters are dependent on all of dayof

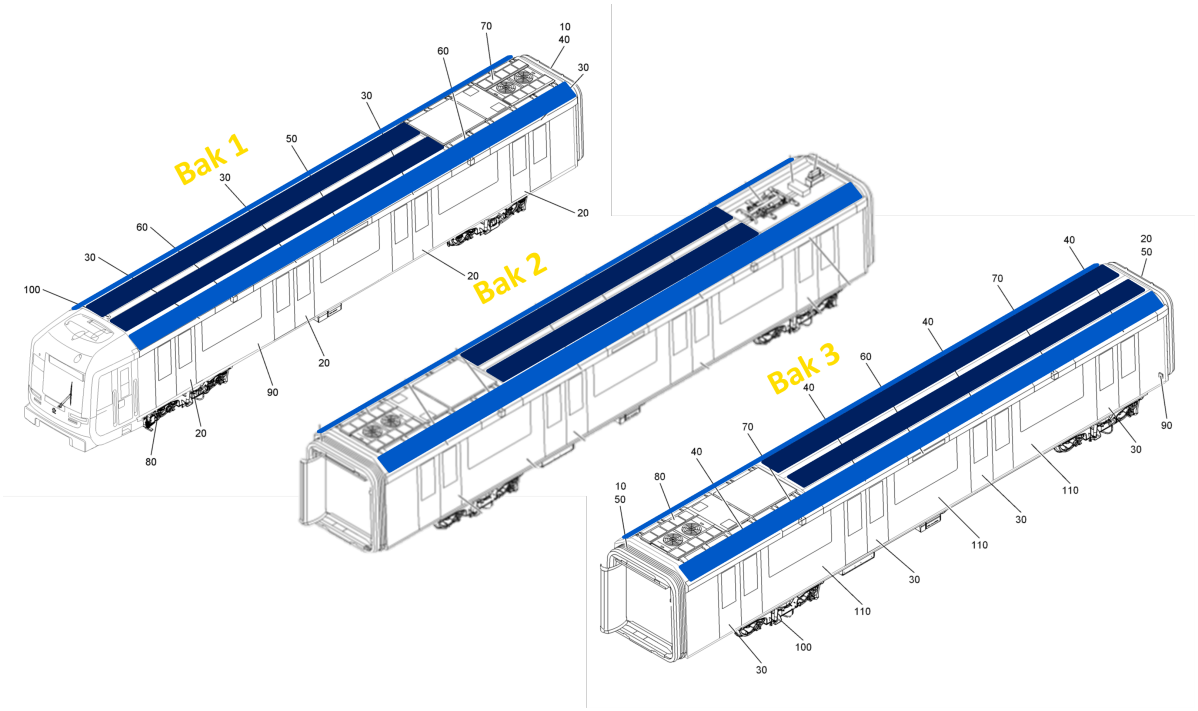

(a) Schematic of the different wagons (”bakken”) of an M5 train covered with PV modules.

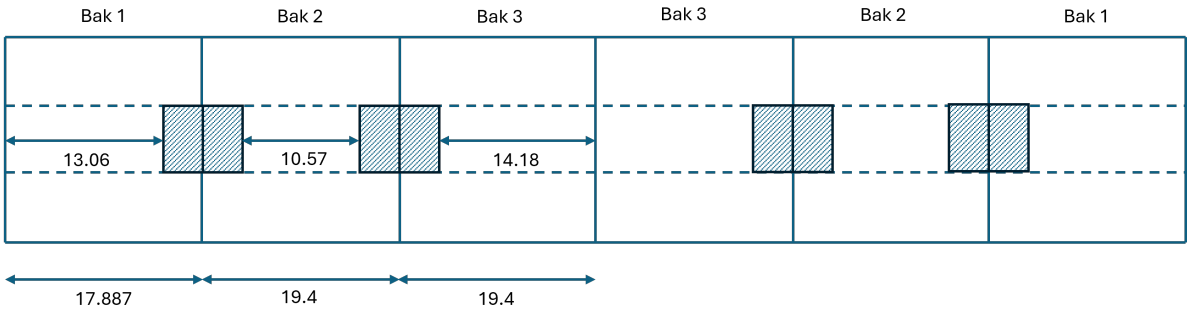

(b) Schematic of the top-view of an M5 train with relevant dimensions in meters.

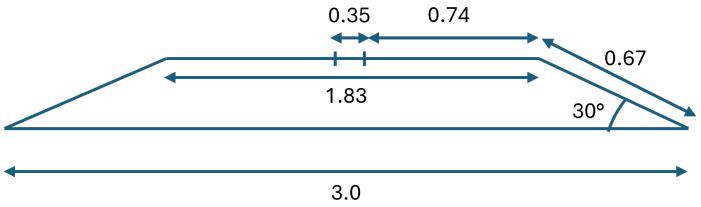

(c) Schematic of the cross-section of the roof of an M5 train with relevant dimensions in meters.

Figure 3.9: Overview of relevant dimensions of an M5 train to find the total area available for PV integration.

4

Results

The MATLAB model has resulted in 1.5 GB of data. The resulting data outputs from a single run are summarized in Table 4.1. In total, with 5 lines running in 2 directions, 10 runs were performed. Each run results in a MATLAB struct with its fields the data outputs as in Table 4.1.

Result	**Unit**	**Value**
ambientT	°C	double[365×5000]
GHI	W/m^2	//
okta	/	//
windDirection	°	//
windSpeed	m/s	//
solarAzimuth	°	//
idxSortYear	/	//
timestamp	HH:MM	duration[365×5000]
efficiency	/	cell1×3 → cell1×3 → double[365×5000]
G_M	W/m^2	//
moduleAzimuth	°	//
modulePower	W	//
SF	/	//
SVF	/	//
T_M	K	cell1×3 → duration[365×5000]
positionX	m	//
positionY	m	//
idxUniqueYear	/	365×1004* double
noon	HH:MM	1×365 duration

Table 4.1: Summary of all the outputs, their units and datatypes for one run of the model. Note that // means the value is the same as the row above.
* This value depends on the specific Line; shown here is Line 50.

The timestamp array is a very important output: most other outputs are based on its dimensions. The timestamp array is a matrix of 365x5000, where the rows represent the days in the year and the columns represent the timestamps that occur on each day. Initially, it was not known how many timestamps would occur on the longest day of the year, so a more than sufficient amount of 5000 was chosen in order not to have the size change dynamically, reducing computation speed. For example, for Line 50 it turns out that on the shortest day of the year, there were 2140 entries and on the longest day 3584, so on subsequent runs, this number may be reduced. The ambient temperature, solar azimuth, GHI, cloud cover, wind direction and wind speed outputs are all reshuffled inputs, but made compatible with the timestamp array. idxSortYear has the same size too. It contains indices that can be used to

reconstruct the unsorted version of the timestamp array. It is used with other arrays as well to make sure each value corresponds to the correct timestamp.
Whereas the meteorological outputs only depend on the timestamp, other outputs depend on the metro line, the train segment and the roof section. These outputs are saved in structs where each layer represents one of these variables. The first layer of cells represents the three train segments (front, middle and back) and the second layer the three rooftop sections (slanted port side, flat, slanted starboard). For example, the shading factor depends on both the train segment and rooftop section, so per run this results in nine arrays of 365x5000. In MATLAB, SF31(31,1313) would represent the shading factor in the 1313th timestamp on the 31st of January on the slanted port side roof section of the back train segment,
The module temperature and the x and y positions of the trains do depend on the train segment, but in order to simplify, was made independent on the roof section.
There are two other unique sized results: idxUniqueYear and noon. idxUniqueYear is a matrix where the rows represent the days in the year and the columns represent the amount of unique timestamps per day. noon is an array containing the timestamp for each day in the year where the Sun has the highest altitude angle.

4.1. Yield

The module power output contains the power during a minute for each roof section of each train segment. This represents the yield of the system. The specific yield in kWh/kWp for each roof section and each line is summarized in Table 4.2.

Metro line and direction	**Port* side**	**Flat**	**Starboard* side**
LINE50IN	529.02	596.41	442.22
LINE50OUT	425.56	583.26	526.85
LINE51IN	294.13	343.11	269.16
LINE51OUT	258.41	332.80	288.83
LINE52IN	82.15	113.42	111.48
LINE52OUT	90.07	91.61	65.71
LINE53IN	124.09	179.22	165.17
LINE53OUT	167.79	182.03	128.46
LINE54IN	144.24	210.43	189.81
LINE54OUT	195.10	218.74	151.67

Table 4.2: Annual yield per line for both directions for each roof section in kWh/kWp/year.
w.r.t. the outbound driving direction

The total potential yield per line in MWh is summarized in Table 4.3.

The yield as a function of the position along the metro tracks is shows in Figure 4.1.

These yield results are discussed in Section 5.1.

Metro line	Yield [MWh]
Line 50	301
Line 51	173
Line 52	79.8
Line 53	91.8
Line 54	108

Table 4.3: Summary of the annual yield per line.

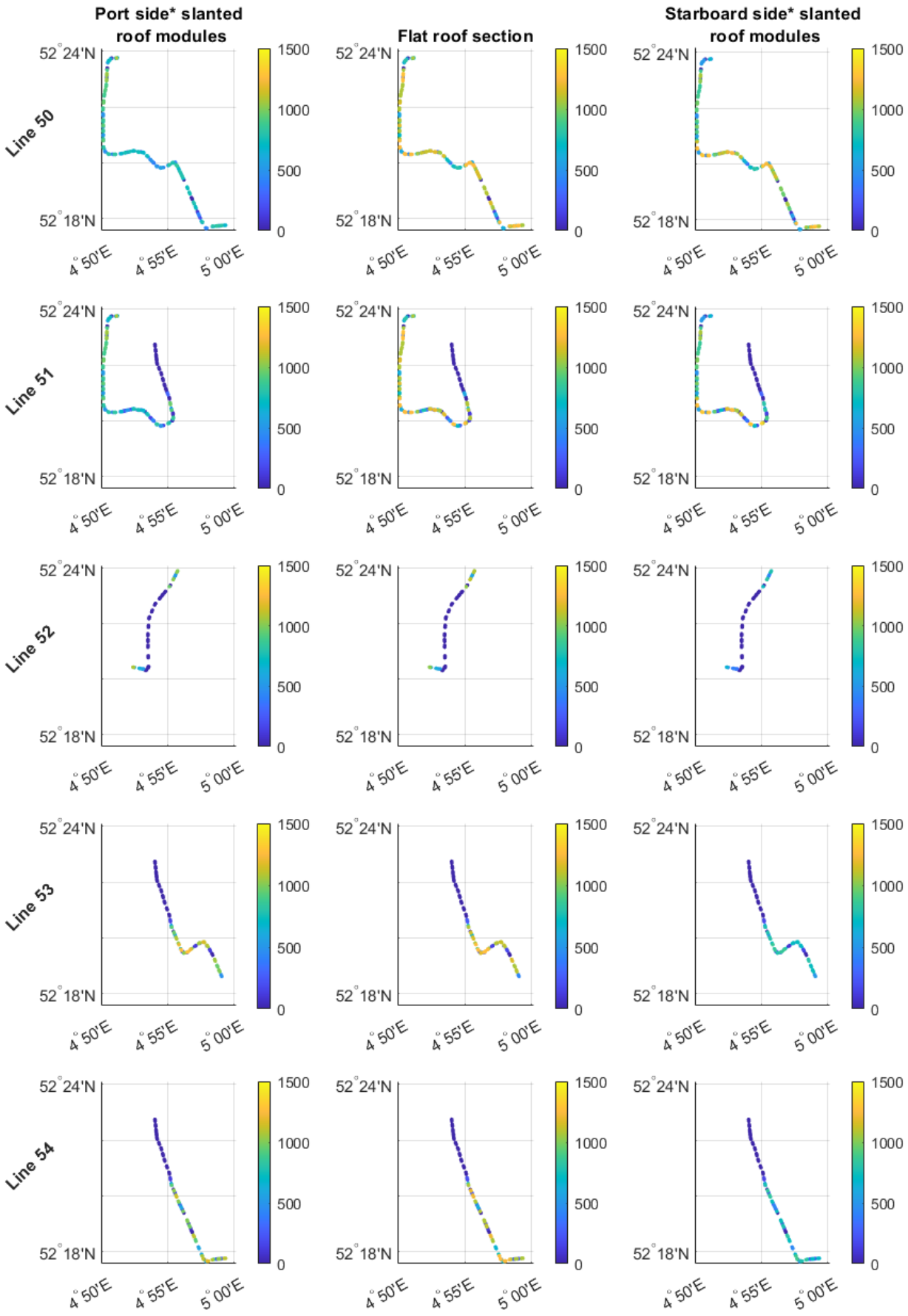

Figure 4.1: Yield in $kWh/m^2/year$ along the metro tracks. The rows represent the metro lines and the columns the tilt of the roof section.
* w.r.t. the outbound driving direction

4.2. Probability Distributions

The probability distributions of some parameters are shows in this section.

The probability distributions of the KNMI inputs of GHI (Figure 4.2), wind speed (Figure 4.4), cloud cover (Figure 4.5) and ambient temperature (Figure 4.3) during 2023 are shown on the next pages.

The probability distributions of timestamps per line are shown in Figure 4.6.

The probability distributions of the yield per timestamp and the SVF for each set of metro line and roof section are shown in Figures 4.7 and 4.8. In both these figures, the red bar shows the relative amount of instances where either the yield or SVF are 0. This represents the amount of timestamps during which the modules are in tunnels, beneath viaducts or at covered train stations. The percentage of total cases is shown as well.

The results of the probability distributions are discussed in Section 5.2.

4.3. Computation speed

The computation time is an important aspect of any computer model. The computation time for each run of the MATLAB model is summarized in Table 4.4. In total, the ten runs required to retrieve all the data, take a total of 899.5 minutes, or about 15 hours.

	Outbound	Inbound
Line 50	133	143
Line 51	103	97.0
Line 52	75.8	80.9
Line 53	59.5	67.1
Line 54	68.5	71.7

Table 4.4: Computation time in minutes per line and driving direction.

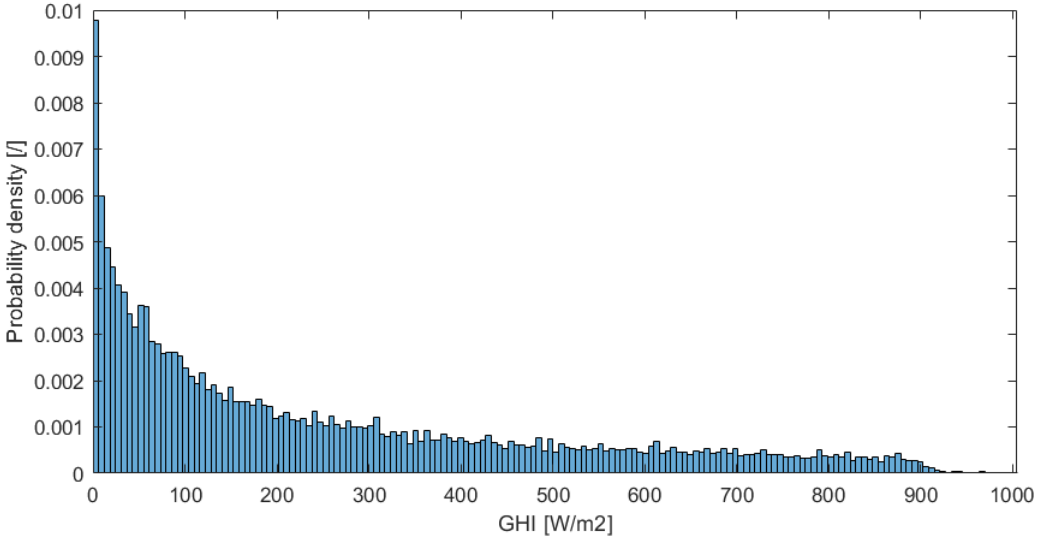

Figure 4.2: Histogram of KNMI GHI data with a binsize of 6.1 W/m^2.

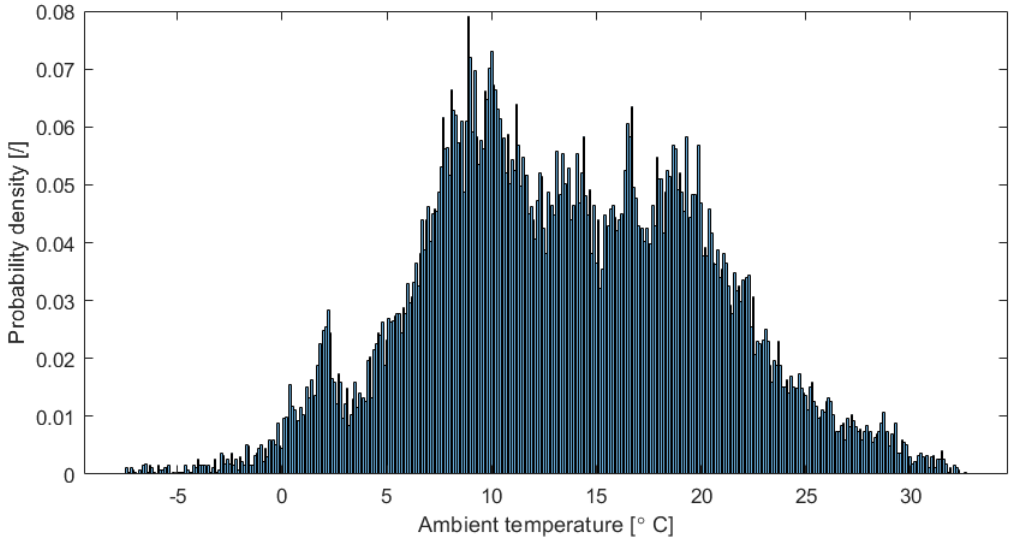

Figure 4.3: Histogram of KNMI ambient temperature data with a binsize of 0.1 $^{\circ}C$.

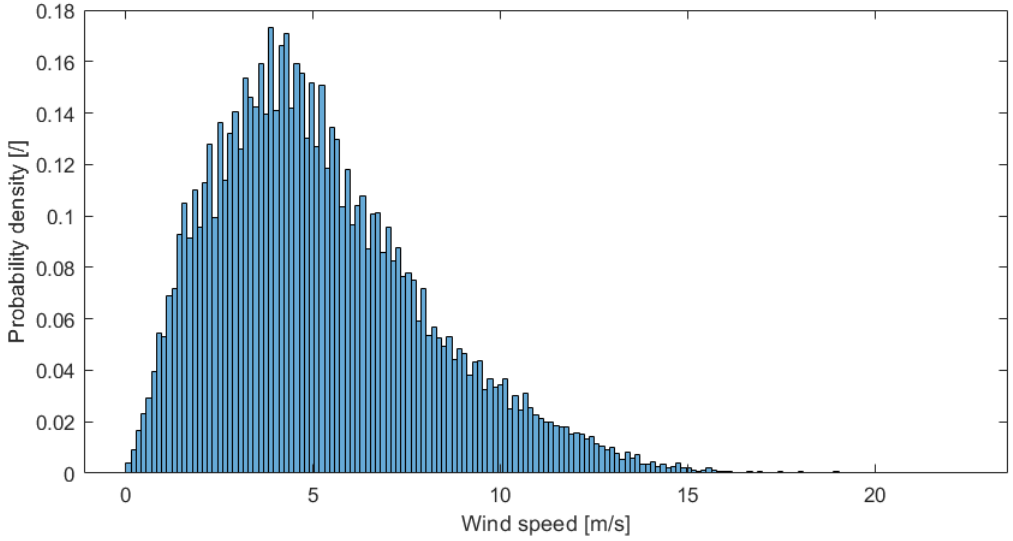

Figure 4.4: Histogram of KNMI wind speed data with a binsize of 0.136 m/s.

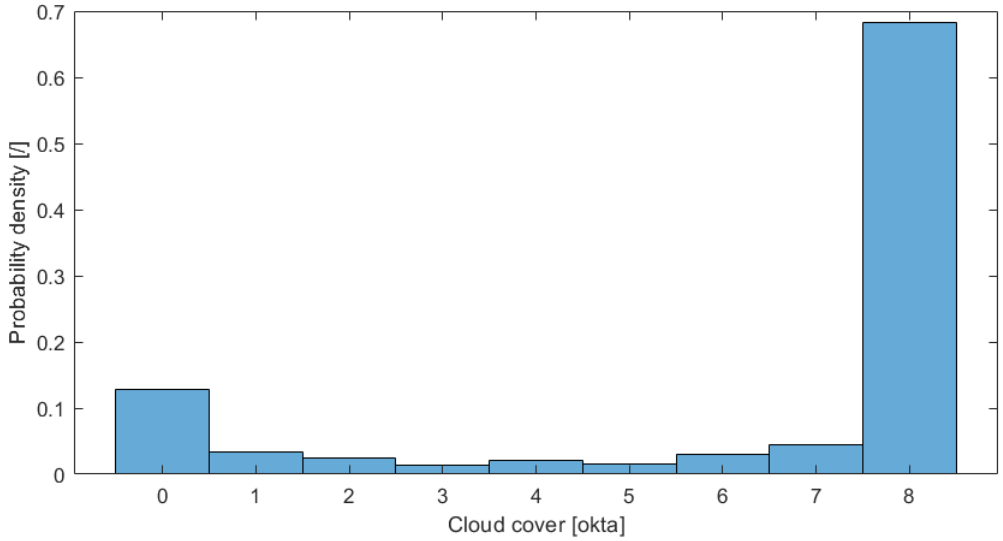

Figure 4.5: Histogram of KNMI cloud cover data with a binsize of 1 $okta$.

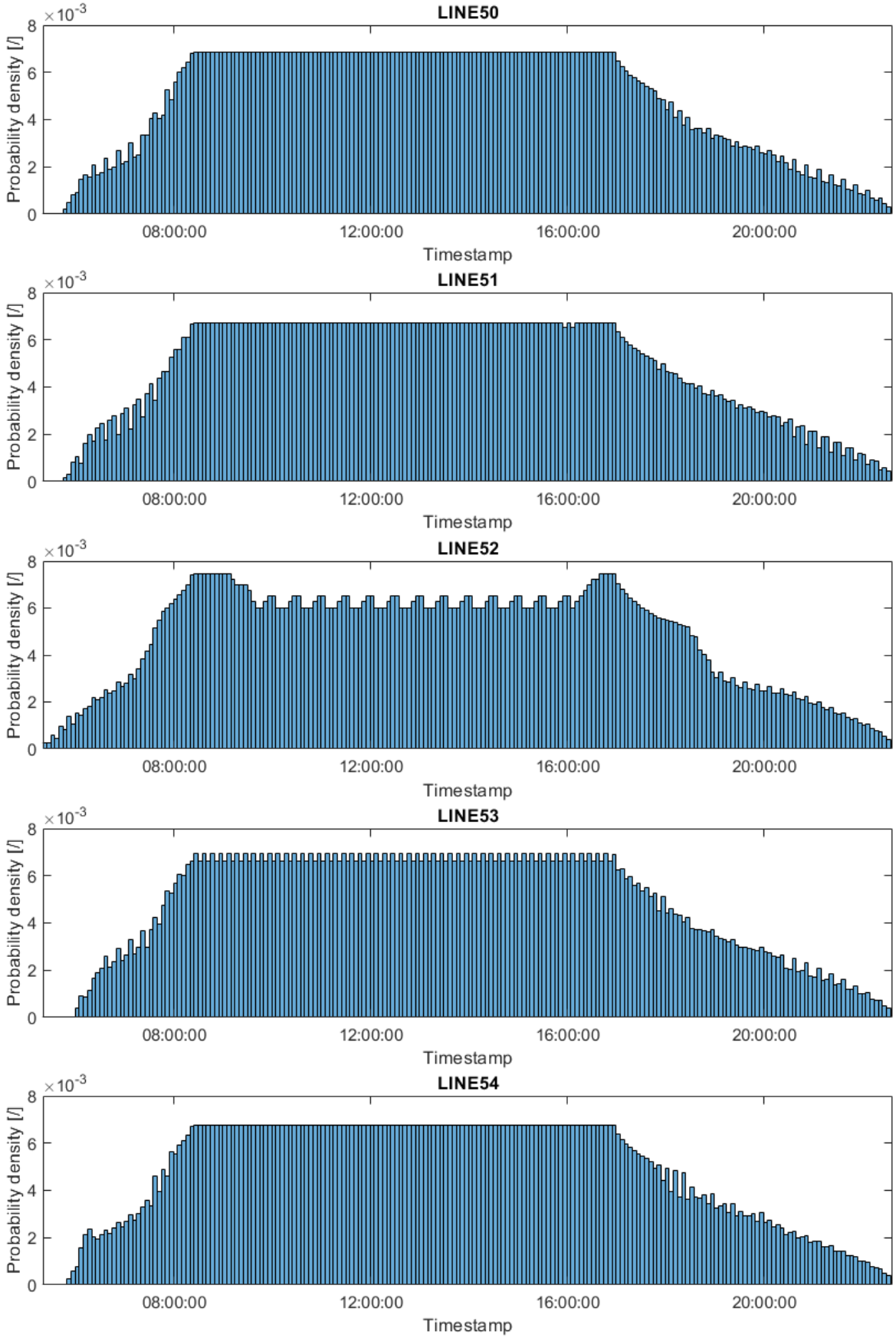

Figure 4.6: Probability distributions of all timestamps per line, bin size = 5 minutes.

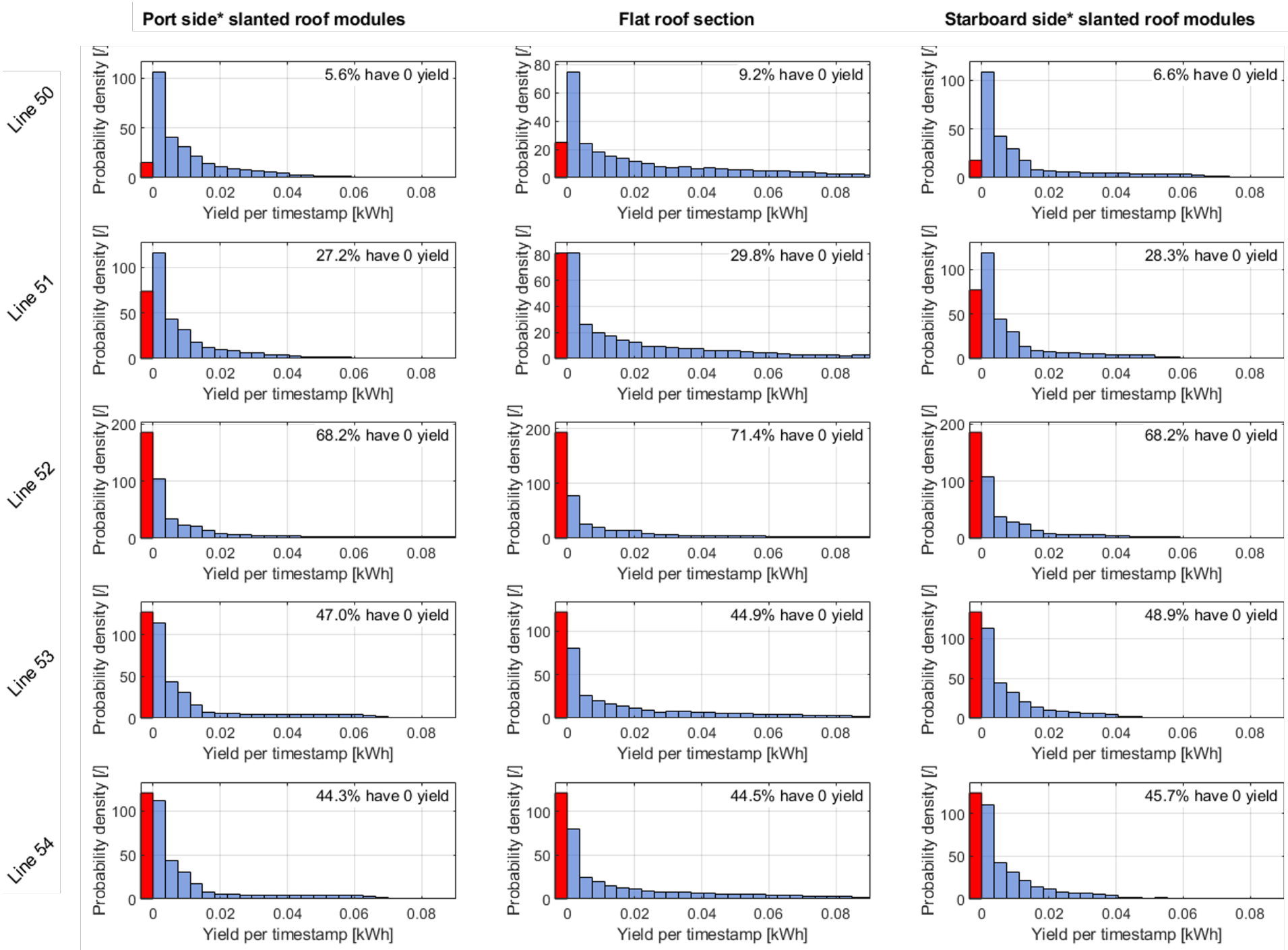

Figure 4.7: Probability distributions of all yields per timestamp, where the rows represent the lines and the columns the roof sections. w.r.t. the outbound driving direction

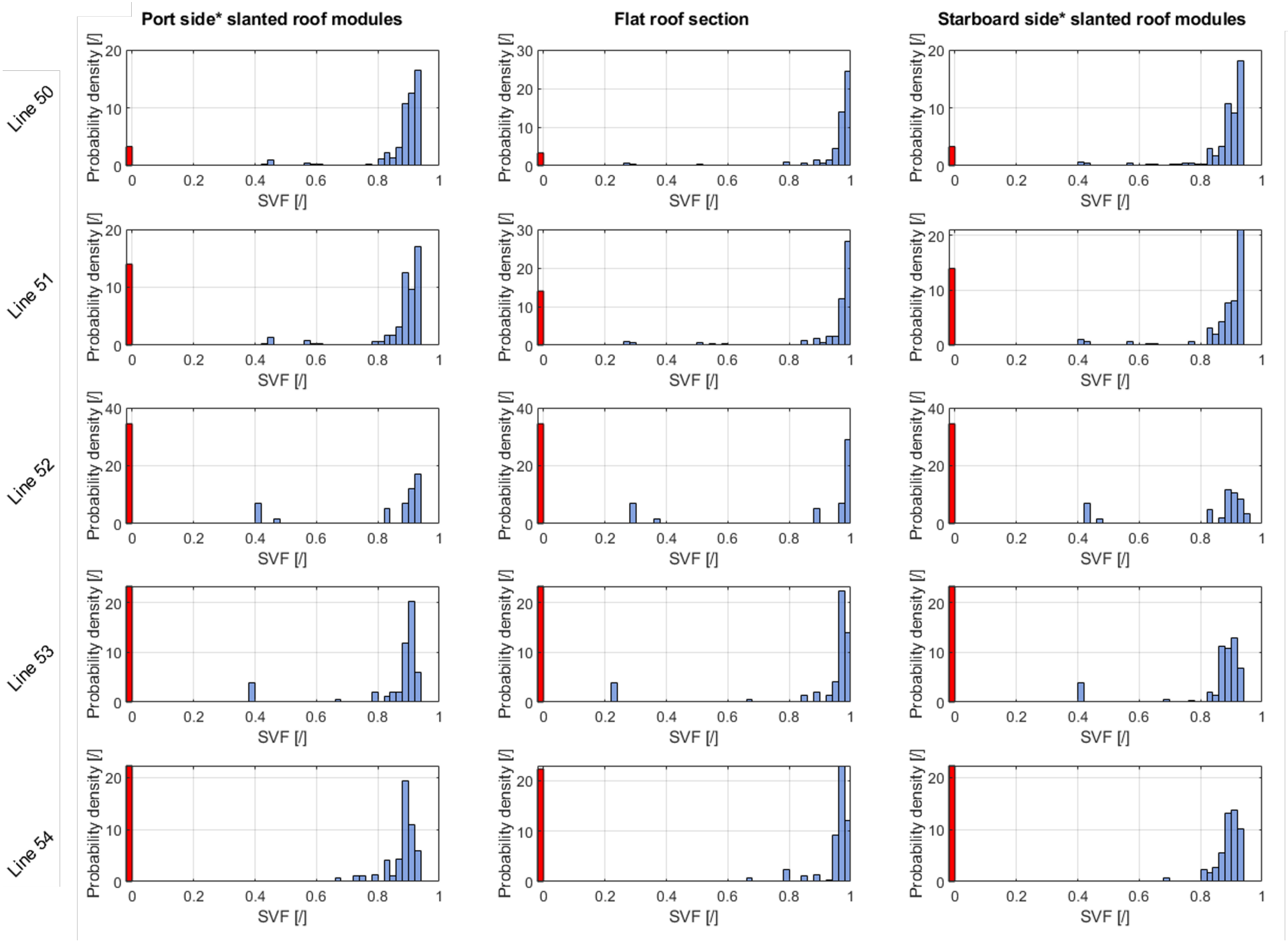

Figure 4.8: Probability distributions of all SVF's, where the rows represent the lines and the columns the roof sections. w.r.t. the outbound driving direction

5

Discussion

5.1. Discussion of yield results

Table 4.2 shows the specific yield in kWh/kWp for each line in either direction distinguishing between roof section. The highest specific yield is reached on the flat roof section on inbound Line 50 trains, with 596.41 kWh/kWp. The lowest specific yield is reached on the starboard side of the outbound Line 52 trains, with 65.713 kWh/kWp. These numbers can be explained by looking at the aboveground percentage of each lines as well as the module orientation w.r.t the driving direction. Line 52 has the lowest aboveground percentage with only 33%, whereas Line 50 is aboveground 100% of the time, not including viaducts and covered metro stations. The yield of flat modules is not affected by the module orientation, but for tilted modules, it is. For Line 50, the modules that are placed on the starboard side w.r.t. the outbound direction are mostly facing South at least partially. For static systems, on these positions, the tilted panels would outperform the flat panels. In this dynamic system however, there are also long stretches of track where the trains run more in a North-South than in a East-West fashion. Along these North-South sections, the panels on the slanted roof sections are facing East and West. For these sections, the flat panels outperform the slanted modules.

It is clear that Line 50 has the highest overall potential specific yield, followed by Line 51, Line 54, Line 53 and Line 52 respectively. This result is also seen in the annual yields per line in MWh as summarized in Table 4.3. In the latter table there is a relatively small difference between the yield of Line 52, 79.8 MWh, and that of Line 53, 91.8 MWh. Compared to Line 52's value, Line 53's annual yield is roughly 15 % larger. Looking at Table 4.2 and comparing their values, Line 53's values are roughly 70 to 80 % larger. The reason for this discrepancy has to do with differences in both the frequency and the size of the trains on both lines. Line 52 exclusively runs M5 trains, whereas Line 53 runs a mix of M4, M5, M7a and M7b. Recalling 3.1, the usable area of M4 is roughly 25 % of M5, M7a roughly 50 % and M7b roughly equal. Regarding the frequency, in 2023, regardless of the time of day, Line 52 ran 8 trains per hour, whereas for the other lines this varied from 4 to 6. Note that in 2024 for Line 52 the frequency of the trains between 07:00-09:00 and 16:00-18:30 was increased to 12 trains per hour, further increasing the total potential yield for this line. The specific yield should remain similar.

In the Netherlands the specific yield amounts to $\sim 850kWh/kWP/year$ on average [23]. Compared to that, the modeled PV installations on trains are strictly lower, but by how much depends on the line. The difference can mostly be attributed to the underground percentage of the lines. Other factors are the amount of timestamps where the tracks are covered by stations or viaducts and the effects of low SVF and SF. As the specific yields of the metro lines are rather low, the economic viability is questionable. The payback time of the system would be longer for systems with lower specific yields. The systems could be subsidized and arguments could be made for their carbon reducing effect and the novel use of available space.

This result from Table 4.2 can also clearly be seen in Figure 4.1. In this figure the yield (in $kWh/m^2/year$) along each metro line distinguishing between the three roof sections is shown. Although it is a result

of the yields that modules would have placed on top of the metro trains, it can also be used to investigate where best to place modules on the side of the tracks. Both for specific locations, as well as for longer stretches of tracks. For this purpose, the results of this research are limited to the three module orientations: flat and tilted 30 degrees with an azimuth perpendicular to the driving direction. It should be noted that some specific yield values are higher than the Dutch average. This is unlikely, so most likely the fault lies with the model. The flat modules show the overall highest yield, yet dependent on the orientation of the vehicle, a tilted module may produce more for specific coordinates where it's orientation is South facing.
Using the results for the tilted modules, the model could be expanded to cover more wagon surfaces with PV modules, namely the walls of the trains on the side of the train that has the higher yield on the tilted modules.

In Figure 4.1 dark blue dots represent locations where the yield is 0 $kWh/m^2/year$. These clearly correspond to the tunnels running below the historic city centre as well as covered train stations and viaducts. For Line 50, roughly in the center of the plot, there is a relatively long blue section for the flat and port side modules that looks slightly different than the same positions on Line 51. The reason this segment is blue, has to do with the SVF and SF values at those positions. A quick look at PDOK for this segment explains the unfavorable SVF and SF values: the metro track dips down go underneath a viaduct. On the West of the viaduct, the railway tracks are to the South and on the East, there is a highway ramp to the South. Both are raised w.r.t. the metro tracks. See Figure 5.1.

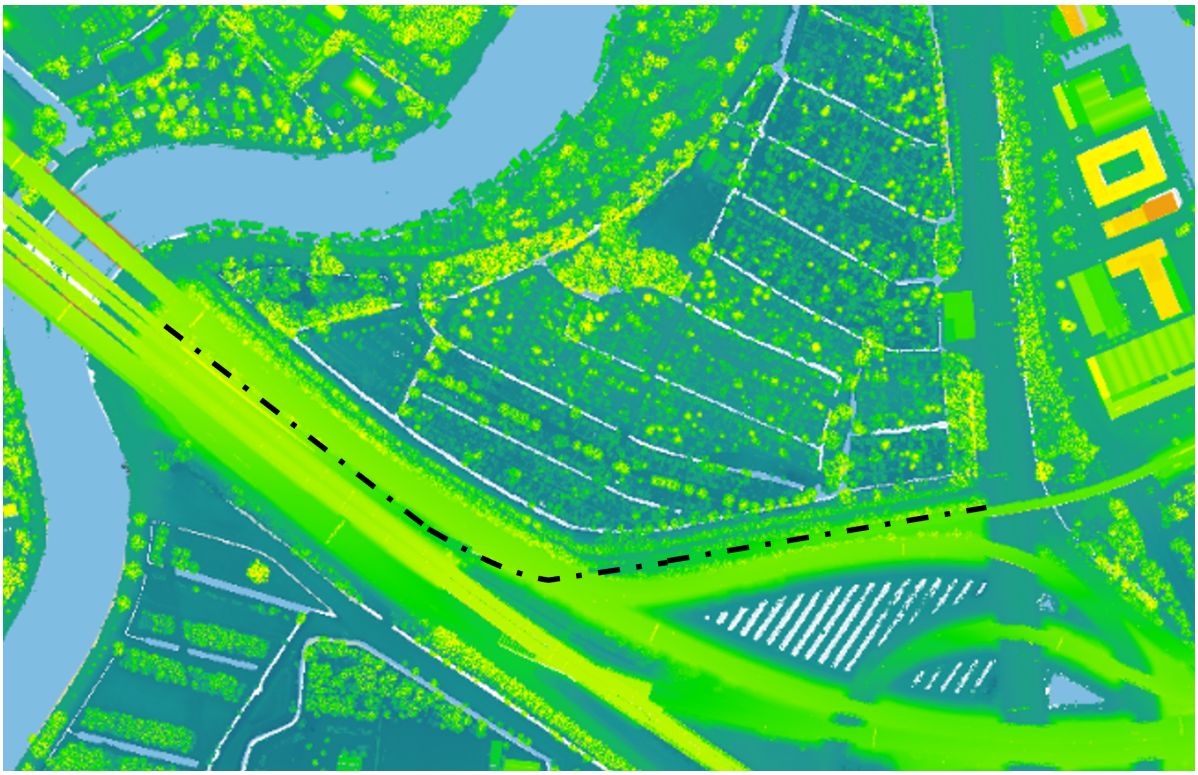

Figure 5.1: Section of PDOK map showing the metro track position for which the annual yield is comparatively low.

In Figure 4.1, positions are often quite close together. The dots representing the yield have a certain size in order to keep the results intelligible. This means that low yield dots could be indiscernibly hidden behind higher yield dots, as the largest values are shown first. An example is shown for flat roof modules for Line 51 in Figure 5.2. Making the dots smaller in order to show all would unfortunately make the results hardly visible, so this approach was still chosen, but this makes it harder to understand if a long stretch of track is actually viable as it may seem like there is a higher yield. A solution would be to either have the possible locations spaced evenly or to cluster the unevenly spaced location into evenly sized and spaced bins.

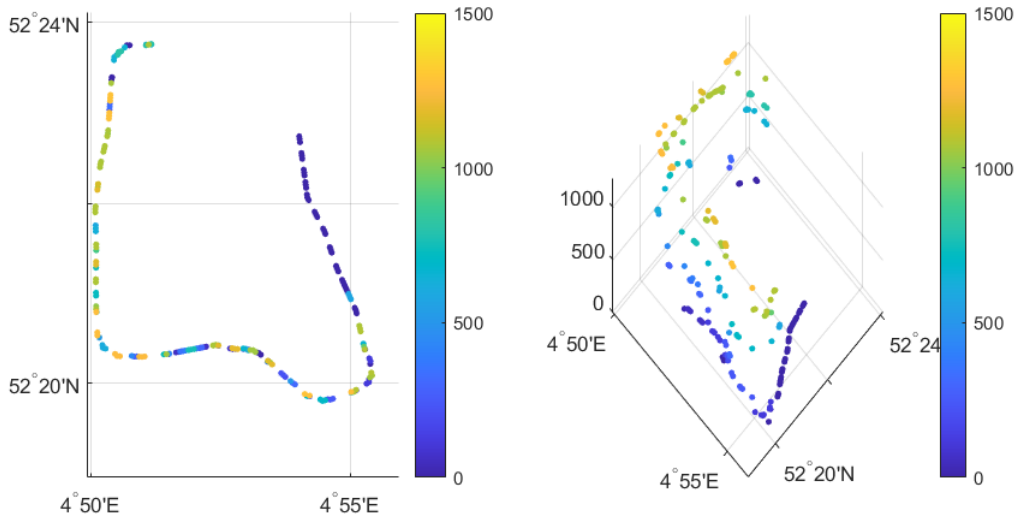

Figure 5.2: A comparison between two viewing angles of the flat roof section Line 51 plot from Figure 4.1, the one on the left is top down and the one the right with both the azimuth and altitude a 45 ○ angle.

5.2. Discussion of probability distributions

Figures 4.2 to 4.5 show the probability distributions of the weather in 2023, using KNMI data. In Figure 4.4, the irregular bin heights mentioned and explained in Section and Appendix B. These plots could provide insight in their effects on the overall results. The same data is also stored for each timestamp„ so the effects could be matched directly to the yield results for the same timestamps.

Figure 4.6 on 31 shows the probability distribution of the timestamps per line for which the model has calculated all results. Few things become clear from these plots. Each line ramps up and winds down the amount of trains running simultaneously until a maximum level. This is what is expected from the frequency data in Table 3.1, except for Line 52. For all lines except 52, the frequency starts at 4 trains an hour, increasing to 6 during the day and going back to 5 before finishing at 4 again. This explains why the slope on the evening side of the distribution is lower than on the morning side. For Line 52, Table 3.1 suggests a continuous level throughout the day, suggesting it would reach its maximum frequency earlier than the other lines. Clearly, these systems need to ramp up and slow down, but in order to explain the difference between Line 52 and the others has to be investigated further. Two other things are noteworthy about Figure 4.6. Firstly, Line 52 shows more trains during rush hour periods in the morning and early evening. As mentioned below Table 3.1, the GVB intended to increase the frequency during rush hour from 8 to 12 trains in 2024. The relative probability density does not show a 2:3 ratio for those hours, but it is reflected to a lesser extent nonetheless. Secondly, there are some irregular spikes. Because of the way the GVB structures its timetables, some timestamps occur more often.
The results from Figure 4.6 could be used in future research to help match load profiles with time dependent power generation distributions.

Figure 4.7 on 32 shows the probability distribution of the yield per timestamp. The plots also show the proportion of cases where the yield is zero. These percentages are shown in the plots and represent the amount of time each roof section per line is covered. They range from 5.6% to 9.2% for Line 50, to about $\sim$ 70% for Line 52. Recall the aboveground percentage of 33% for Line 52 from Table 3.1, these numbers correspond quite well. For lines 50, 51, 53 and 54 the model results are lower than the aboveground percentages in Table 3.1. As they are aboveground for longer stretches of time, the effects of viaducts and covered train stations become more apparent. It is odd to see that the percentages in Figure 4.7 are higher for the flat roof sections than for the slanted ones; if anything, it is expected to be the other way around. In order to investigate why these values are higher for the flat modules than for the slanted ones, further investigation is needed.

Figure 4.8 on 33 shows the probability distribution of the SVF per timestamp. The plots also show the proportion of cases where the SVF is zero. These cases represent the timestamps where the train is in a tunnel a covered by a viaduct or station roof. The discussion on their meaning is the same as with the yield per timestamp as described in the paragraph above, or as seen in Figure 4.7 on 32. It is clear that the maximum SVF reached is (close to) 1 for each of the flat roof sections. For the slanted sections, the maximum SVF is limited to 0.933 by geometry, which is represented in the plots as well. The specific locations corresponding to the lower SVF peaks likely correspond to canyon-esque locations. For example, as explained in Section 5.1 and as seen in an example in Figure 5.1, the metro tracks are sometimes surrounded by high walls on either side when the tracks dip down to go underneath a viaduct. For Line 52 specifically, there is a relatively long canyon-esque section when the metro track emerges from the tunnel running below het IJ. See Figure 5.3. This is most likely the explanation of the low-SVF peaks at $\sim$0.4 for slanted modules and $\sim$ 0.3 for flat modules. The reason that this peak is lower for flat modules than for slanted modules, which also clearly applies to Line 53 and if looked at carefully also for Lines 50 and 51, has to be investigated further.

Figure 5.3: Section of PDOK map showing the section of Line 52 for which the annual yield is comparatively low.

5.3. Recommendations for the model

This section discusses possible recommendations in order to improve the results as well as the computation speed of the model. It does so for all the submodels: the skyline, metro position, weather, temperature and yield models respectively.

5.3.1. Skyline model

The skyline model has a resolution of 0.5 $^\circ$ which is already quite fine. Also the scanning radius of 300 m is sufficient in an urban environment. Improving the resolution or radius further would not improve the skyline profiles significantly.

In the current model, the skylines are generated for a list of coordinates retrieved from the Gemeente Amsterdam website (see Appendix A). Aboveground, this amounts to 456 unevenly spaced coordinates sets defining the positions of all metro tracks. Changing to a method where these positions are evenly spaced, could be useful for multiple reason. For one, matching the metro train positions to skylines in the skyline library would be more realistic. Interpretation of the results of the annual yield plots in Figure 4.1 for determining the exact locations and stretches of track where modules could be placed,

would become more useful.
One as of yet unresolved issue with the skyline model is that of the close-wall correction that Keijzer's thesis mentioned [19]. Implementation of his algorithm was attempted, but was not entirely successful. Some spikes still show up in the skyline profiles. An example of the skyline profile at the Isolatorweg station is shown in Figure 5.4.The open corridors along the metro tracks running East-West as well as the underpass running North-South are clearly visible. The speaks towards the East likely represent the utility poles visible on the station platform. These are relatively high, but mostly close to the observer resulting in these spikes. The jagged, pointy section towards the South-West-West direction however should most likely have been smoothed out if Keijzer's algorithm was implemented correctly.
A recommendation for improving the skyline profiles and skipping the modeling altogether would be to use horicatcher technology. A horicatcher is a camera device that converts fish-eye images of the sky to skyline profiles. In conjunction with a GPS device, placing these on trains on each of the lines, could replace the skyline model altogether and improve the results too.

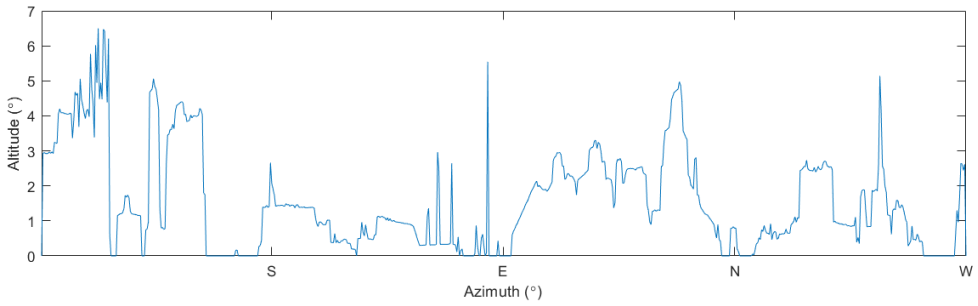

Figure 5.4: Skyline profile at Isolatorweg station (52°23'43"N, 4°51'03"E)

5.3.2. Metro position model

The current method of determining the metro wagon positions as a function of time consists of interpolating between the departure times from the metro stations and those locations. Between each position a time interval of 1-min is taken between each point. The smallest difference between departure times on consequent stations is 1-min so this interval is the largest possible interval, or crudest possible resolution. Smaller intervals would lead to a finer resolution, but increase the computation speed drastically. In the end, the model is proof of concept and increasing the resolution would be relatively easy.
Using departure times in order to determine the location of the trains is just a modeling approach. It would be more accurate to use archived live tracking data of the metro trains. This would include the effects of variable wagon speeds as well as of delays on the wagon positions and, indirectly, the skylines experienced at those times. The use of live tracking data was attempted for this research. Unfortunately, the datasets provided by colleagues at the Civil Engineering and Geosciences faculty did not contain any live tracking of the GVB metro trains. They did contain live tracking data for RET metro trains, as well as those of buses and trams within the GVB network, just not for the GVB metro trains. The reason as to why these datasets did not seem to contain the locations of GVB metro trains is as of yet unknown, but it may have to do with a migration of data from KV6 to NeTEx. The datasets used that contain archived live tracking data are KV6 and NeTEx datasets. A phone call with a 9292 employee confirmed that the data should exist as it is the basis of the live tracking service in the 9292 app. It should be noted however, that even with live tracking data, the temporal resolution is not necessarily compatible with the research purposes such that a form of interpolation may still be necessary. The KV6 data investigated showed unequal intervals.

Outside daylight hours, calculations are performed for timestamps 1.5 hours before sunrise and after sunset. This was done in order to take into account diffuse light still being present. In hindsight, the time interval with which the daylight hours are exceeded, might be quite excessive, given the very limited contribution of the diffuse light at those timestamps to the overall yield. Additionally, it was a flat 1.5 hours throughout the year, but it should be made dependent on the time of year. In summer this time interval should be longer than in the winter. Making these time intervals shorter, can increase computation speed without losing significant yield.

The metro position model is based on the same weekday timetable, repeated for every day of the year. The model currently does not distinguish between the different timetables for weekdays, weekends, the summer period and periods of planned maintenance.

5.3.3. Weather model

In this research, the input data was limited to KNMI data from one weather station for the entirety of 2023. In order to improve the statistical analysis, it could prove beneficial to increase the size of the dataset. This could be done by using averaged data for more years. Another possibility is using a weighted average for the measurements of multiple KNMI weather stations surrounding Amsterdam, as now the closest one was used. A combination of both would be even better.

5.3.4. Temperature model

The fluid-dynamic model was chosen as temperature model. It takes into account convection cooling, which can be beneficial for the efficiency of the PV modules. The results of the temperature show room for improvement. For example, in some instances, the module temperatures are below ambient temperature. As the temperature response is modeled to be instantaneous, this is impossible. It occurred solely in summer months and not in winter months. Also it did not occur for entire days, just for a couple intervals during the day. It was remedied by taking the module temperature for those timestamps to be equal to the ambient temperature instead. Arguably the temperature ought to be much higher than ambient in the summer months, but given the multitude of possible origins, this approach was chosen. The efficiencies used by the model are thus likely overestimated, resulting in overestimated power outputs.

In order to prevent large nonphysical jumps in module temperature, a maximum temperature increase could be implemented. Due to problems with implementation in the fluid-dynamic model and time constraints, this was not implemented. However, the algorithm ought to be similar to that below. This algorithm also prevents module temperatures from being smaller than the ambient temperature.

$$T_M(i) = \begin{cases} T_a(i) & \text{if } T_M(i) < T_a(i) \\ T_M(i-1) + \Delta T_{M,max}(i) & \text{if } |T_M(i) - T_M(i-1)| > |\Delta T_{M,max}(i)| \\ T_M(i) & \text{otherwise} \end{cases}$$

$$\Delta T_{M,max}(i) = \frac{\Delta E}{C_M} = \frac{\Delta G_M * 60s}{C_M} \tag{5.1}$$

where $C_M = 2918 J/K$ for a 0.51 m^2 monocrystalline PV module [24]. Scale this, section wise, to the area of the modules used and this will provide a rough approximation of the maximum temperature change in a minute. Applying thermal lag modeling could reduce errors in module temperatures.

5.3.5. Yield model

Each roof section of each train segment contains an array of modules. The distinction between roof sections and train segments was made to account for the fact that, in contrast to for example a single module on a car, different parts of the train would experience different skylines and shades. However, for the roof sections, which are still quite large compared to a single module, the SVF and SF for these arrays are calculated as if they are condensed in a single point. So in the model, each roof section experiences the same SVF and SF uniformly. Partial shading of arrays is very important for the yield results, but is not account for. Subdividing the train into three segments rather than just the one, is a proof of concept that the model can handle subdivisions. It would be relatively easy to subdivide this even finer to the module level, but this would drastically increase the computation time. However, this would also require the skyline library to increase similarly. Otherwise, if the model would match multiple modules locations to the same skyline, the SVF and SF would still be the same. Additionally, going even finer than the module level would be necessary to include effects of partial shading. This has been done for a VIPV system by Macías et al [7] and includes LiDAR and ray tracing to make this possible.

Due to time constraints, little to no time was spent on the technical feasibility of retrofitting the modules on the trains. No research was performed into the Balance of System (BoS). The components of this BoS (e.g. inverter, cables or batteries) are subject to certain efficiencies lwoer the PV system output. These are now not taken into account, although a rough estimate of its efficiency of 90% could have been used [5].

5.3.6. Customized solar modules

In order to maximize roof usage, custom solar modules were designed to cover as much surface area as possible. While commissioning a company to manufacture these custom modules is likely to be a costly endeavor and consequently might be a crude assumption, this is not the primary focus of this research. The overarching goal is to explore the feasibility of integrating PV modules on metro trains by any means possible, rather than to optimize for commercial viability at this stage. Crystalline silicon modules were chosen for this study due to their high overall energy yield. Alternative technologies such as thin-film modules may offer easier and more cost-effective customization, but would likely result in a lower overall yield.

5.4. General recommendations

The model could be used with the GVB trams and/or buses as well. As the sources for track coordinates contain information both for its metro trains, trams and buses, it would be relatively easy to expand perform the same research for those as well.

For proper probability distribution analysis, two things are recommended. First, fit distributions known to apply to specific parameters in order to validate the results. Second, the distributions in kWh/kWp ought to be be investigated as there a exists a research gap. To this end the model should be adapted to calculate the yield per vehicle and not per timestamp. Another flaw of the model is that the maximum capacity in kWp was not stored, so in order to investigate the above-mentioned, this should be adapted.

6

Conclusion

This thesis explored the integration of PV modules on the roof surfaces of Amsterdam's metro wagons, with the goal of assessing the solar energy generation potential and patterns of dynamic PV systems. The outset of this thesis was to answer the following research questions:

1. How could metro wagons be covered in PV modules and which challenges arise when doing so?
2. Would this result in enough energy to account for the entire metro network, and if not, what part?
3. Which alterations to the metro power network infrastructure are needed to this end?
4. Given that the Amsterdam metro network is $\sim$80% aboveground and that metro networks are usually underground, how would the energy yield and power series change for networks with different aboveground percentages?
5. Therefore, another possible path for the research is to explore the probability distribution curve of PV power production on top of trains.

Throughout the course of the research it became clear that not all of these questions could be answered or even approximated easily. One reason is time constraints; building the MATLAB model from scratch took more time than expected. Prioritizing the yield potential of the PV system, technical analysis of implementing PV modules on the trains and research into the accompanying, appropriate BoS components was left out. Another reason is the availability of information. There is little information publicly available on the power infrastructure surrounding the GVB metro network. The same goes for other metro networks. Even upon reaching out to GVB and consulting experts in the field, this information was not retrieved. One relevant example would be the amount of electricity the network consumes, another one the design of the electronic circuits on the back of the metro trains.

6.1. Model

A modular and adaptable model was developed, taking into account spatial, meteorological, and technical parameters specific to the Amsterdam metro network. These include a skyline model using AHN LiDAR data as input, a metro position model interpolated from the GVB timetables, a weather model using KNMI data as input, a temperature model based on the fluid-dynamic model and finally, a yield model using the outputs from the other models as well as custom module parameters. The model should be seen as a proof of concept of the feasibility study of PV module integration. Many submodels can be refined relatively easily improving realism, but coming at the cost of computation speed. Subdividing the train segments and roof sections even smaller and increasing the temporal resolution of the metro position model are straightforward. Additionally, this would require an increase in the spatial resolution of the skyline model, thus an expansion of the skyline library that currently contains 456 entries.
Regarding the metro position model, the usage of live tracking data would increase realism of the vehicle speeds and positions. For the temperature model, certain anomalies such as module temperatures

dropping below ambient levels suggests improvements to the fluid-dynamic model or the implementation in the overall model could be increased. Implementing a temperature response model would further enhance realism. Partial shading effects on arrays, which can significantly impact output in real-world conditions. Further segmentation of the train is recommended.

6.2. Potential Yield

Looking at the results in Tables 4.2 and 4.3 as well as Figures 4.1 and Figure 4.7, it became evident that the potential yield is highly dependent on a combination of factors: the percentage of time the train operates aboveground, the orientation and tilt of the modules relative to the driving direction, and the SVF and SF. The flat roof section of inbound Line 50 trains yielded the highest specific output at 596.41 kWh/kWp, while the starboard-tilted modules of outbound Line 52 trains performed the worst, with only 65.71 kWh/kWp. These results can be largely attributed to the differences in the aboveground percentage. Figure 4.7 shows the percentage of time each line is fully covered. Unlike static PV systems, dynamic systems face rapidly changing azimuth angles and shading conditions, which can cause the tilted panels to underperform compared to flat-mounted alternatives, under otherwise equal conditions. While the maximum yields obtained in this study are lower than the Dutch average of □850$kWh/kWp/year$ for static systems [23], the variation across lines and roof sections illustrates that meaningful generation is possible in specific cases, albeit for dynamic implementation on entire lines or for static implementation on specific locations alongside the tracks.The data in Tables 4.2 and 4.3 also reveals that the specific yield per line does not directly correspond to the total annual yield, as train frequency and wagon composition play a significant role. For instance, Line 52 runs more frequent services and uses a uniform M5 fleet, while other lines deploy a mix of vehicle types with varying usable roof area, affecting the annual energy output.

6.3. Probability Distributions

Figures 4.6, 4.7 and 4.8 show ways in which large amounts of data for complex systems, can be visualized and made intuitive. The values in these plots, are mostly as expected from theory.
In order to investigate the research gap of kWh/kWp distributions for an ensemble of modules, the model needs to be adapted. The yields should be calculated on a per vehicle basis, compared to the current method of finding these values for each timestamp. Additionally, the kWp values should be stored in the same fashion as the other data.

6.4. Outlook

While the economic feasibility of metro-integrated PV systems is currently limited due to relatively low specific yields and high installation complexity, the concept represents a novel and underexplored use of dynamic PV systems. Such systems can contribute to broader sustainability goals by utilizing otherwise unused surfaces in the urban landscape. Custom module designs, though costly, demonstrate the possibility of maximizing usable area, and future innovations in lightweight or flexible PV technologies may reduce cost and improve integration ease.

References

[1] Rijksdienst voor Ondernemend Nederland. *Klimaat- en Energieverkenning 2024: klimaatdoel 2030 raakt uit zicht*. Retrieved from https://www.rvo.nl/nieuws/klimaat-en-energieverkenning-2024 (Accessed on 24-04-2025). 2024.

[2] GVB. *GVB draagt bij aan nieuw Amsterdams Klimaatakkoord*. Retrieved from https://over.gvb.nl/nieuws/gvb-draagt-bij-aan-amsterdams-klimaatakkoord (Accessed on 24-04-2025). June 24, 2019.

[3] GVB. *Elektrische bussen opladen met remenergie van Noord/Zuidlijn*. Retrieved from https://over.gvb.nl/nieuws/elektrische-bussen-opladen-met-remenergie-van-noord-zuidlijn/ (Accessed on 24-04-2025). May 2, 2024.

[4] GVB. *GVB ondertekent akkoord voor aanpak vol stroomnet*. Retrieved from https://over.gvb.nl/nieuws/gvb-ondertekent-akkoord-voor-aanpak-vol-stroomnet/ (Accessed on 24-04-2025). Apr. 1, 2025.

[5] Arno H. M. Smets et al. *Solar Energy: The Physics and Engineering of Photovoltaic Conversion, Technologies and Systems*. UIT Cambridge Ltd., 2016.

[6] International Energy Agency. *Solar PV*. Retrieved from https://www.iea.org/energy-system/renewables/solar-pv (Accessed on 15-04-2025). IEA. 2024.

[7] Javier Macías et al. "On the optimization of the interconnection of photovoltaic modules integrated in vehicles". In: *iScience* 27.6 (2024), p. 110089.

[8] Kenji Araki, Yasuyuki Ota, and Kensuke Nishioka. "Testing and rating of vehicle-integrated photovoltaics: Scientific background". In: *Solar Energy Materials and Solar Cells* 280 (2025), p. 113241.

[9] Mahdi Sarvi and Ali Azadian. "A comprehensive review and classified comparison of MPPT algorithms in PV systems". In: *Energy Systems* 13.2 (2022), pp. 281–320.

[10] Philipp Hoth et al. "Vehicle-Integrated Photovoltaics—A Case Study for Berlin". In: *World Electric Vehicle Journal* 15.3 (2024), p. 113.

[11] Yasaman Darvishpour et al. "Integration of Rooftop Solar PV on Trains: Comparative Analysis of MPPT Methods for Auxiliary Power Supply of Locomotives in Milan". In: *Electronics* 13.17 (2024), p. 3537.

[12] Agam Shah. "Sun Train: World's First Fully Solar-Powered Train on Track". In: *Mechanical Engineering* 140.4 (Apr. 2018), pp. 10–11.

[13] M. Shravanth Vasisht et al. "Rail coaches with rooftop solar photovoltaic systems: A feasibility study". In: *Energy* 118 (2017), pp. 684–691.

[14] Zhujun Chen et al. "Using existing infrastructures of high-speed railways for photovoltaic electricity generation". In: *Resources, Conservation and Recycling* 178 (2022), p. 106091.

[15] GVB. *GVB Holding NV Jaarverslag*. Retrieved from https://over.gvb.nl/content/uploads/2024/05/Jaarverslag-GVB-2023-1.pdf (Accessed on: 13-01-2025). 2024.

[16] GVB. *Vervoerplan 2024-I*. Retrieved from https://over.gvb.nl/content/uploads/2023/09/Concept-Vervoerplan-2024-deel-1.pdf (Accessed on: 16-01-2025). 2023.

[17] Hesan Ziar Dora de Jong. "Photovoltaic Potential of the Dutch Inland Shipping Fleet An Experimentally Validated Method to Simulate the Power Series from Vessel-Integrated Photovoltaics". In: *Solar RRL* 7 (2022).

[18] Carlotta Ferri et al. "Mapping the photovoltaic potential of the roads including the effect of traffic". In: *Renewable Energy* 182 (2022), pp. 427–442.

[19] M.C. Keijzer. “A Multi-Surface Reflected Irradiance Model for Pyranometer Corrections and PV Yield Calculations in Complex Urban Geometries”. MA thesis. Delft University of Technology, 2019.

[20] Railway Technology. *Alstom Metropolis Trains*. Retrieved from https://www.railway-technology.com/projects/alstom-metropolis-trains/ (Accessed on 16-07-2024. 2014.

[21] Francesco Antonio Tiano et al. “Evaluation of the potential of solar photovoltaic panels installed on vehicle body including temperature effect on efficiency”. In: *eTransportation* 5 (2020), p. 100067.

[22] Sandeep Mishra. “Selection Map for PV Module Installation Based on Shading Tolerability and Temperature Coefficient”. MA thesis. Delft University of Technology, 2018.

[23] Karen Brandenburg et al. *Onderzoek naar productiefactoren zonnestroom in 2022*. Tech. rep. Retrieved from https://www.cbs.nl/nl-nl/longread/diversen/2023/onderzoek-naar-productiefactoren-zonnestroom-in-2022?onepage=true (Accessed: 2025-01-23). Centraal Bureau voor de Statistiek (CBS), Dec. 2023.

[24] A. D. Jones and C. P. Underwood. “A Thermal Model for Photovoltaic Systems”. In: *Solar Energy* 70.4 (2001), pp. 349–359.

A

Input data URL's

AHN LiDAR data:
`https://service.pdok.nl/rws/ahn/atom/dsm_05m.xml`
These files were used:
R_25BZ2.tif
R_25EZ1.tif
R_25DN2.tif
R_25GN1.tif
R_25GN2.tif
R_25GZ1.tif
R_25GZ2.tif

KNMI meteorological data:
This data had to be accessed by calling the KNMI website's api. This was done with MATLAB. These are the api URLs accessed:
`https://api.dataplatform.knmi.nl/open-data/v1/datasets/zonneschijnduur_en_straling/versions/1.0/files/`
`https://api.dataplatform.knmi.nl/open-data/v1/datasets/vochtigheid_en_temperatuur/versions/1.0/files/`
`https://api.dataplatform.knmi.nl/open-data/v1/datasets/bewolkingsgegevens/versions/1.0/files/`
`https://api.dataplatform.knmi.nl/open-data/v1/datasets/windgegevens/versions/1.0/files/`

GVB metro track data:
`https://maps.amsterdam.nl/open_geodata/`
Verkeer & Infrastructuur –> Tram- en metrolijnen 2024–> Download csv Excel

GVB timetables:
`https://reisinfo.gvb.nl/reisinformatie/haltes-en-dienstregeling`

B

Correspondence KNMI

Outlook

Re: Potentiële fout bij data verzameling windsnelheden bij meetstation Schiphol

Van Open Data (KNMI) [R E D A C T E D]
Datum Di 6-8-2024 14:07
Tot Tristan ten Napel [R E D A C T E D]

Beste Tristan,

Er gaat zeker iets met jouw melding gedaan worden, echter kan het wel nog even duren voordat dit volledig opgelost is.

Momenteel is de huidige meetapparatuur toe aan vervanging. Voor het vervangen is een project gaande welke uit meerdere fases bestaat. Enkel de meetapparatuur vervangen zal het probleem nog niet geheel oplossen.

In de toekomst willen we de processing volledig off-loaden van de edge (sensoren en bijbehorende apparatuur). Door te off-loaden is er meer flexibiliteit waardoor jouw melding volledig opgelost kan worden.

Nogmaals dank voor het rapporteren.

Met vriendelijke groet,
XXXXX
Open Data team KNMI
.....
Royal Netherlands Meteorological Institute (KNMI)
Ministry of Infrastructure and Water Management
Utrechtseweg 297 | 3731 GA De Bilt
Postbus 201 | 3730 AE De Bilt | The Netherlands
.....

From: Tristan ten Napel [R E D A C T E D]
Sent: Thursday, August 1, 2024 5:04:51 PM
To: Open Data (KNMI)
Subject: Re: Potentiële fout bij data verzameling windsnelheden bij meetstation Schiphol

Beste XXXXX,

Bedankt voor de terugkoppeling. Duidelijk en erg interessant om te lezen waar de oorsprong van de gaten zit!

Ik kan me voorstellen dat het geen prioriteit heeft, maar ik was nog benieuwd of dit in de toekomst naar aanleiding van mijn melding aangepast gaat worden.

Met vriendelijke groet,
Tristan ten Napel

Van: Open Data (KNMI)[R E D A C T E D]
Verzonden: donderdag 1 augustus 2024 09:38
Aan: Tristan ten Napel [R E D A C T E D]
Onderwerp: Re: Potentiële fout bij data verzameling windsnelheden bij meetstation Schiphol

Beste Tristan,

Bedankt voor de heldere uitleg en de daarbij behorende data en broncode.

We zijn op onderzoek uitgegaan om jouw vraag te kunnen antwoorden en hebben het Sensor Interface Team(SIT) erbij betrokken. Zij kunnen ons meer vertellen hoe de sensoren meten en geven het volgende aan:

Merk op dat 0.01 m/s de output resolutie van de SIAM is voor windsnelheid.

De SIAM meet intern met zgn counts/3sec 1 count/3sec= 198cm/omwenteling*omw/32*1/3=2.0625 cm/s maar rekent verder in cm/s (volgens de oude SIAM specificatie). De resolutie van de sample waarde zou dan inderdaad 0.02 m/s zijn maar de 10-minuut gemiddelde zou een hogere resolutie moeten hebben, tenzij de SIAM intern in counts rekent en we pas bij het samenstellen van de SIAM string naar cm/s converteren!? Ik vermoed dat de SIAM in counts (als integer) rekent omdat in de nieuwe SIAM memo diverse criteria in counts worden gegeven.
In dat geval is de resolutie van de windsnelheid 2.0625 cm/s terwijl we rapporteren met 1 cm/s resolutie waardoor gaten in het histogram met 0.01 m/s resolutie ontstaan.

Yes, the wind speed is processed using integer counts on the SIAM. Wind speed is only converted to cm/s during SIAM message generation.

Dit verklaart het gaten in het histogram voor windsnelheid met een 0.01 m/s resolutie. De SIAM rekent intern met een 1 count resolutie. In de SIAM string worden de resultaten weggeschreven in cm/s of 0.01 m/s resolutie maar omdat 1 count correspondeert met 2.0625 cm/s zullen enkele 0.01 m/s bins leeg zijn.

Met vriendelijke groet,
XXXXX
Open Data team KNMI
.....
Royal Netherlands Meteorological Institute (KNMI)
Ministry of Infrastructure and Water Management
Utrechtseweg 297 | 3731 GA De Bilt
Postbus 201 | 3730 AE De Bilt | The Netherlands
.....

From: Tristan ten Napel [R E D A C T E D]
Sent: Wednesday, July 3, 2024 3:50:05 PM
To: Open Data (KNMI)
Subject: Potentiële fout bij data verzameling windsnelheden bij meetstation Schiphol

Beste lezer,

Tijdens mijn onderzoek waarbij ik KNMI windsnelheid data gebruik van het meetstation Schiphol 18Cm27, heb ik ontdekt dat er waarschijnlijk iets misgaat bij de data verzameling. Het histogram dat ik van de data heb gemaakt laat onnatuurlijk gedrag zien: sommige *bins* bevatten aanzienlijk veel minder *counts* dan hun buren. Dit gebeurt bijv. bij de bins met alle windsnelheden die afgerond 3.6 m/s, 4.3 m/s en 4.9 m/s zijn. Dit is nog enigszins periodiek ook. Zie onderstaande afbeelding.

De windsnelheden worden verstrekt als getallen met twee decimalen. Sommige getallen blijken helemaal niet voor te komen en daar zit ook nog een bepaalde periodiciteit in:
4.96 en 4.98 komen niet voor terwijl 4.97 en 4.99 respectievelijk 168 en 150 keer voorkomen. Hoewel het om en om lijkt vindt er af en toe een shift plaats: zo komen zowel 4.93 en 4.94 beide niet voor, maar hun buren wel.

Ik dacht ik laat het even weten. Misschien hebben jullie er wat aan. Ik heb de data en het script wat ik heb gebruikt bijgevoegd.

Met vriendelijke groet,
Tristan ten Napel Probability Distribution Wind Speed.zip

C

PV module datasheet

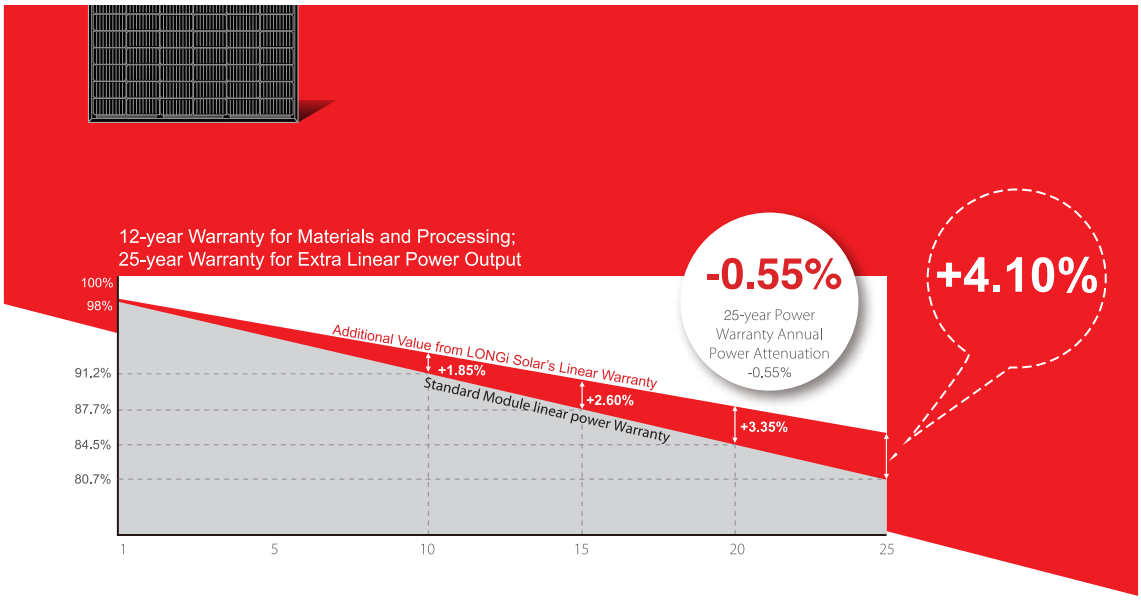

Complete System and Product Certifications

IEC 61215, IEC 61730, UL 61730

ISO 9001:2008: ISO Quality Management System

ISO 14001: 2004: ISO Environment Management System

TS62941: Guideline for module design qualification and type approval

OHSAS 18001: 2007 Occupational Health and Safety

* Specifications subject to technical changes and tests.
LONGi Solar reserves the right of interpretation.

Positive power tolerance (0 ~ +5W) guaranteed

High module conversion efficiency (up to 20.3%)

Slower power degradation enabled by Low LID Mono PERC technology: first year <2%, 0.55% year 2-25

Solid PID resistance ensured by solar cell process optimization and careful module BOM selection

Reduced resistive loss with lower operating current

Higher energy yield with lower operating temperature

Reduced hot spot risk with optimized electrical design and lower operating current

LONGi

Room 801, Tower 3, Lujiazui Financial Plaza, No.826 Century Avenue, Pudong Shanghai, 200120, China
Tel: +86-21-80162606 E-mail: module@longi-silicon.com Facebook: www.facebook.com/LONGi Solar

20200414V11 for EU DG only

LR4-60HPB **345~370M**

Design (mm)

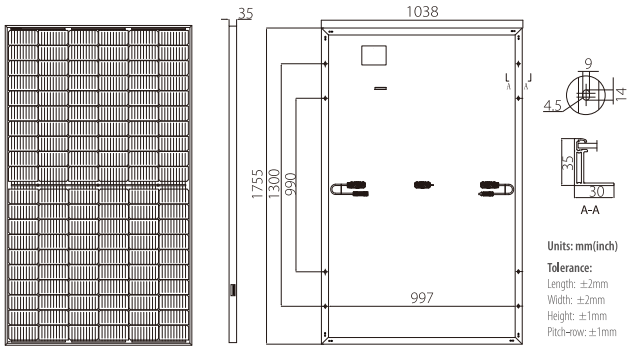

Mechanical Parameters

Cell Orientation: 120（6×20）
Junction Box: IP68, three diodes
Output Cable: 4mm², 1200mm in length
(for EU DG)
Connector: MC-MC4
Glass: Single glass
3.2mm coated tempered glass
Frame: Anodized aluminum alloy frame
Weight: 19.5kg
Dimension: 1755×1038×35mm
Packaging: 30pcs per pallet
180pcs per 20'GP
780pcs per 40'HC

Operating Parameters

Operational Temperature: -40℃~+85℃
Power Output Tolerance: 0~+5 W
Voc and Isc Tolerance: ±3%
Maximum System Voltage: DC1000V (IEC/UL)
Maximum Series Fuse Rating: 20A
Nominal Operating Cell Temperature: 45±2℃
Safety Class: Class Ⅱ
Fire Rating: UL type 1 or 2

Electrical Characteristics

Test uncertainty for Pmax: ±3%

Model Number	LR4-60HPB-345M		LR4-60HPB-350M		LR4-60HPB-355M		LR4-60HPB-360M		LR4-60HPB-365M		LR4-60HPB-370M	
Testing Condition	STC	NOCT	STC	NOCT	STC	NOCT	STC	NOCT	STC	NOCT	STC	NOCT
Maximum Power (Pmax/W)	345	257.6	350	261.4	355	265.1	360	268.8	365	272.6	370	276.3
Open Circuit Voltage (Voc/V)	40.2	37.7	40.4	37.9	40.6	38.1	40.8	38.2	41.0	38.4	41.2	38.6
Short Circuit Current (Isc/A)	11.06	8.95	11.16	9.02	11.25	9.09	11.33	9.16	11.41	9.23	11.50	9.30
Voltage at Maximum Power (Vmp/V)	34.2	31.8	34.4	32.0	34.6	32.2	34.8	32.4	35.0	32.6	35.2	32.8
Current at Maximum Power (Imp/A)	10.09	8.09	10.18	8.16	10.27	8.23	10.35	8.30	10.43	8.36	10.52	8.43
Module Efficiency(%)	18.9		19.2		19.5		19.8		20.0		20.3	

STC (Standard Testing Conditions): Irradiance 1000W/m², Cell Temperature 25℃, Spectra at AM1.5

NOCT (Nominal Operating Cell Temperature): Irradiance 800W/m², Ambient Temperature 20℃, Spectra at AM1.5, Wind at 1m/S

Temperature Ratings (STC)

Temperature Coefficient of Isc	+0.048%/℃
Temperature Coefficient of Voc	-0.270%/℃
Temperature Coefficient of Pmax	-0.350%/℃

Mechanical Loading

Front Side Maximum Static Loading	5400Pa
Rear Side Maximum Static Loading	2400Pa
Hailstone Test	25mm Hailstone at the speed of 23m/s

I-V Curve

Current-Voltage Curve (LR4-60HPB-360M)

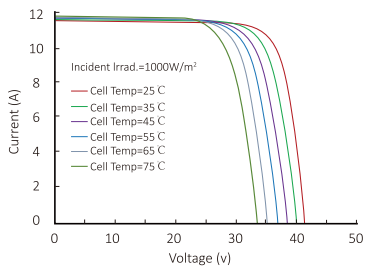

Power-Voltage Curve (LR4-60HPB-360M)

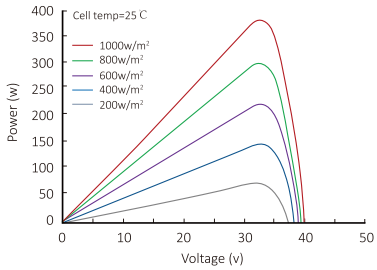

Current-Voltage Curve (LR4-60HPB-360M)

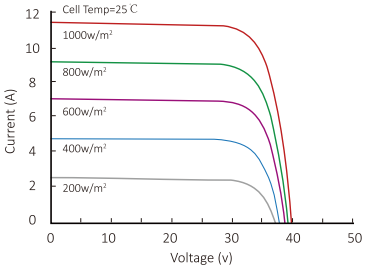

LONGi

Room 801, Tower 3, Lujiazui Financial Plaza, No.826 Century Avenue, Pudong Shanghai, 200120, China
Tel: +86-21-80162606 E-mail: module@longi-silicon.com Facebook: www.facebook.com/LONGi Solar

20200414V11 for EU DG only

D

Skyline sub-model flowchart

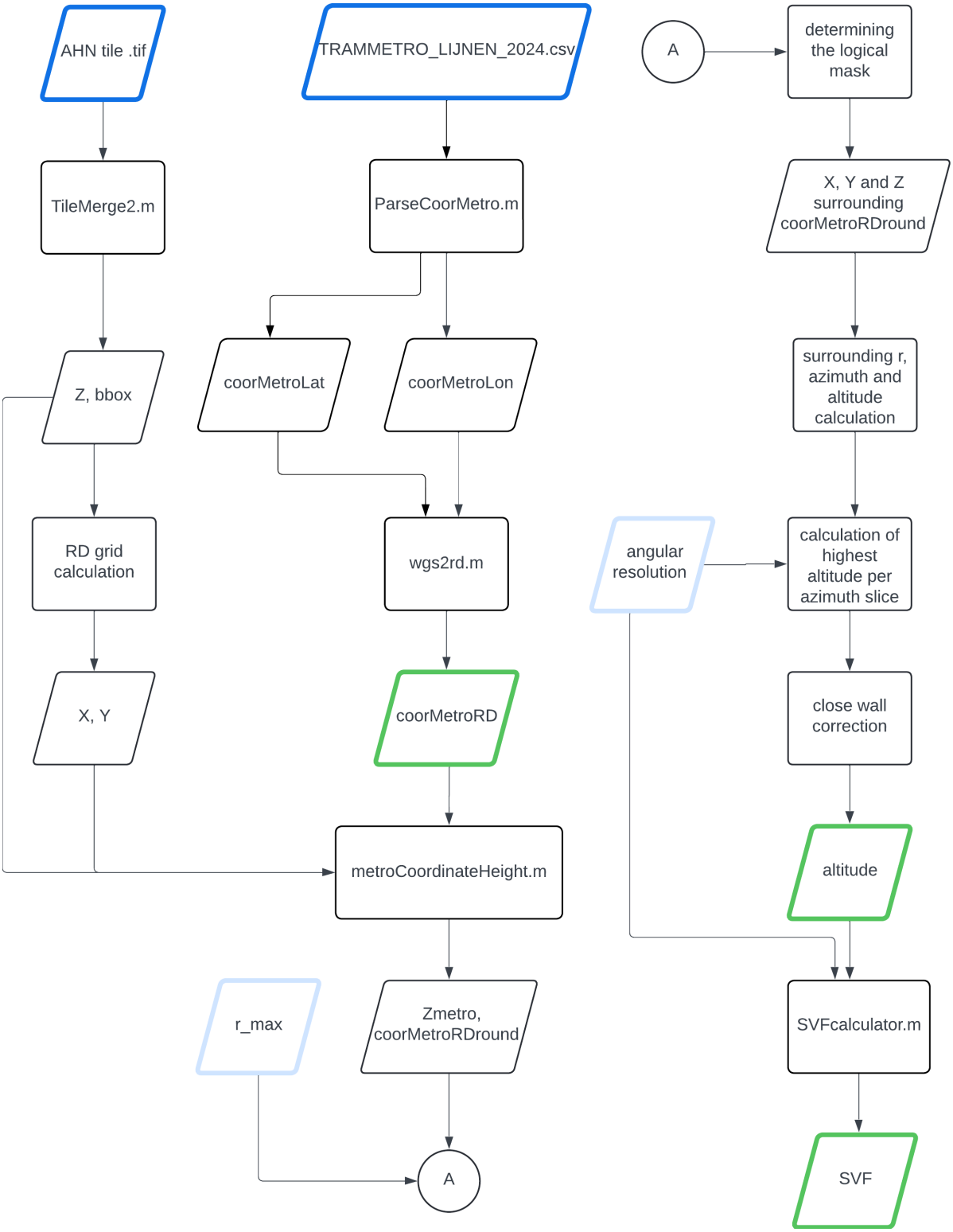

E

Perez model

The equations used to model the circumsolar and horizontal brightening contributions to the diffuse irradiance component, use Perez coeffients. For these equations, see chapter 2.3.

$$F_1 = \max\left[0, \left(f_{11} + f_{12}\Delta + \frac{1-\theta_z}{180^\circ} f_{13}\right)\right] \tag{E.1}$$

$$F_2 = f_{21} + f_{22}\Delta + \frac{\pi\theta_z}{180^\circ} f_{23}\epsilon \tag{E.2}$$

$$\Delta = \frac{DHI \times AM_a}{E_a} \tag{E.3}$$

$$E_a = E_{sc} \times \left(\frac{R_{av}}{R}\right)^2 \tag{E.4}$$

$$\left(\frac{R_{av}}{R}\right)^2 = (100011 + 3422.1\cos(b) + 128\sin(b) + 71.9\cos(2b) + 7.7\sin(2b)) \times 10^{-5} \tag{E.5}$$

$$b = 2\pi\frac{DOY}{365} \text{ radians} \tag{E.6}$$

In these equations, the variables are as follows:

- θ_z is the solar zenith angle, which is equal to 90◦ minus the solar altitude
- E_a is the extraterrestrial, Sun intensity at the top of the atmosphere
- E_{sc} is the solar constant $1367\ \mathrm{W/m^2}$
- κ is the sky clearness constant of 1.041
- AM_a is the absolute air mass
- ε is related to the cloud cover [okta] bins in the table below
- DOY is the day of the year
- R_{av} is the averaged distance to the sun from the Earth
- R is the distance to the sun from the Earth at a specified time

Table E.1: Table E.1: Perez model coefficients

bin	f_{11}	f_{12}	f_{13}	f_{21}	f_{22}	f_{23}
1	-0.008	0.588	-0.062	-0.06	0.072	-0.022
2	0.13	0.683	-0.151	-0.019	0.066	-0.029
3	0.33	0.487	-0.221	0.055	-0.064	-0.026
4	0.568	0.187	-0.295	0.109	-0.152	-0.014
5	0.873	-0.392	-0.362	0.226	-0.462	0.001
6	1.132	-1.237	-0.412	0.288	-0.823	0.056
7	1.06	-1.6	-0.359	0.264	-1.127	0.131
8	0.678	-0.327	-0.25	0.156	-1.377	0.251